OpenFOAM® Journal

Volume 4 [Full Papers], Pages 1–25
ISSN: 2753-8168

Validation of High Speed Reactive Flow Solver in OpenFOAM® with Detailed Chemistry

Vigneshwaran Sankar[1,2], Karl P. Chatelain[1,2,*], Josué Melguizo-Gavilanes[3,4], and Deanna A. Lacoste[1,2]

[1]Mechanical Engineering Program, Physical Science and Engineering Division (PSE), King Abdullah University of Science and Technology (KAUST), Thuwal 23955-6900, Saudi Arabia

[2]CCRC, King Abdullah University of Science and Technology (KAUST), Thuwal, 23955-6900, Saudi Arabia

[3]Institut Pprime, UPR 3346, CNRS, ENSMA, University of Poitiers, Futuroscope-Chasseneuil, France

[4]Shell Global Solutions B. V., Major Hazards Management, Energy Transition Center, Amsterdam, The Netherlands

Email address: karl.chatelain@kaust.edu.sa

DOI: https://doi.org/10.51560/ofj.v4.125
Results with version(s): OpenFOAM® v2012
Repository: https://github.com/Vigneshwaran-Sankar/reactingPimpleCentralFoam-for-detonations

Abstract. An OpenFOAM® based hybrid-central solver called `reactingPimpleCentralFoam` is validated to compute hydrogen-based detonations. This solver is a pressure-based semi-implicit compressible flow solver based on *central-upwind* schemes of Kurganov and Tadmor, and possesses the features of standard OpenFOAM® solvers namely, `rhoCentralFoam`, `reactingFoam` and `pimpleFoam`. The Kurganov & Tadmor schemes are used for flux splitting to solve the high-speed compressible regimes with/without hydrodynamic discontinuities. In this work, we present the validation results that were obtained from one-dimensional (1D) and two-dimensional (2D) simulations with detailed chemistry. We consider three different mixtures that fall into the categories of weakly unstable mixture ($2H_2 + O_2 + 3.76Ar$ and $2H_2 + O_2 + 10Ar$), and moderately unstable mixture ($2H_2 + O_2 + 3.76N_2$), based on their approximate effective activation energy. We performed the numerical simulations in both laboratory frame of reference (LFR) and shock-attached frame of reference (SFR) for the 1D cases. The 1D simulation results obtained agree well with the steady-state calculations of Zel'dovich von Neumann Döring (ZND) simulations with an average error below 1% in all cases. For the 2D simulations, circular hot-spots were used to perturb the initially-planar detonations to develop into spatio-temporally unstable detonation fronts. The convergence is declared when the speed of the front stabilizes near the CJ speed (Chapman-Jouguet), specifically within a 2% deviation and the regularity of cellular pattern on the numerical smoke foils reaches a steady state. We have verified from our preliminary studies that the SFR-based simulations are computationally cheaper in comparison to the LFR simulations and that the required grid resolution is always lesser in the former than the latter to reach the same level of accuracy (in terms of speed of the detonation front and cell sizes from the numerical smoke foil). We have also verified that at least 24 points per induction zone length (for weakly unstable mixture) and 40 points per induction zone length (for moderately unstable mixture) are required to sufficiently resolve detonation structures that are independent of grid size, boundary and initial conditions. A further reduction in computational cost of approximately 50% is achieved by using non-uniform grids, which converge effectively to the same solutions in comparison to the results from twice the number of grids with uniform resolution.

1. Introduction

Generally, the modes of combustion front propagation can be classified into two categories based on their speed: detonation and deflagration, each with its own complexities when it comes to numerical simulation [1]. In deflagration mode, combustion wave propagates mainly through diffusion. The speed of the flame front is subsonic with respect to the quiescent fresh gas. While in the detonation mode, combustion occurs with the reaction front moving at speeds faster than the speed of sound relative to the unreacted gas. This movement is driven by a shock wave that compresses the gas ahead, elevating both its temperature and pressure to the ignition point. This coupling between the shock wave and reaction front makes a self-sustained detonation front. The simulation of detonation presents several challenges

* Corresponding author

Received: 17 October 2023, Accepted: 21 December 2023, Published: 5 February 2024

mainly because of its multi-dimensional nature, inherent unsteadiness, complex chemical kinetics with detailed reaction mechanisms, wide spectrum of length and time scales, accurate prediction of shock wave propagation and so on [2]. These factors contribute to the high computational cost and the difficulties associated with simulating detonations [1,3–6].

Experimental investigation of detonations started about a century ago [3]. The majority of experimental characterizations of canonical detonations have been performed using time series of pressure traces, smoke foils, or by conducting front visualizations with techniques such as schlieren [7–9], chemiluminescence [9,10], or planar laser-induced fluorescence (PLIF) [7,11–13]. Using these measurement techniques, characteristic length scales of detonations such as the cell width (λ), the cell length (L), and more recently the induction zone length (Δ_i) [11,12] have been investigated. The latter one is a proof-of-concept to estimate Δ_i using NO-PLIF with 2% of error margin.

Detonation simulations have been performed extensively in the last few decades focusing on several aspects such as, the canonical detonation problem [4,14–23], numerical issues [6], detonation transmission in complex domains [24, 25] and so on, due to their applicability in fields like propulsion, safety in hydrogen handling, and energy generation. After reviewing a good number of representative literature in the numerical detonation field, a concise review is presented here. Oran et al. [4] examined gas phase detonations in hydrogen-air mixtures under atmospheric conditions using a one-step Arrhenius reaction kinetics model. They observed a reasonable agreement between the numerical and experimental cell width (λ). This agreement is expected since simulations with simplified chemistry typically involve parameter tuning, with the mean cell width ($\bar{\lambda}$) serving as the fitting target. In a separate investigation, Oran et al. [14] conducted a numerical analysis of a highly diluted stoichiometric hydrogen-oxygen mixture with 70% argon at very low pressure (6.67 kPa) with a detailed reaction model. Interestingly, the cell size reported in their study differed from the experimental value by nearly threefold. This disparity can be attributed to the fact that when developing detailed mechanisms, the primary focus is often on matching experimentally measured ignition delay times (τ_{ign}), obtained under deflagration conditions, rather than accurately reproducing cell widths. Moreover, the detonation simulations are highly sensitive to the grid sizes that are being used. Predictions of shock configurations and reaction, become highly inaccurate when the resolution of the numerical grid drops below 20 points per reaction zone length of the steady detonation [26] in the lab-frame of reference with one-step chemistry. As the resolution is decreased further, the quality of the solution rapidly deteriorates. Attempting to identify the physical structure, evolution, and impact of transverse waves on reaction, using such under-resolved calculations is extremely challenging and poses a significant risk of analyzing nonphysical results [26]. Mével et al. [16] developed and implemented a laser-induced fluorescence (LIF) model to directly perform one-to-one comparison between inviscid detonation simulations and experimental OH-PLIF visualizations, conducted on argon diluted hydrogen-oxygen mixtures. While a qualitative agreement between the experimental and numerical fields was obtained after simulating the LIF process, the numerical cell size was found to be approximately half the size of the experimental measurements. Marcantoni et al. validated their OpenFOAM® based in-house solver called `rhoCentralRfFoam` [20] and further investigated the solver's capability to compute cellular structures in confined detonations in 2D lab-frame simulations, using wave interactions from ignition points as perturbations [21]. They reported good correlation between the experiment and simulation in terms of detonation cell structure for a argon diluted hydrogen mixture.

Several studies pertaining to 3D gaseous detonation also report similar discrepancies between the simulated and experimental cell sizes [27–30]. The major missing physics between the 2D and 3D simulations were identified to be the complex vortical structures behind the detonation front which could have an enhanced influence on burning the fresh gas pockets [29], however this study was performed using 1-step Arrhenius chemistry. 3D simulation reveals the qualitative features of realistic detonation such as slapping waves, rectangular and diagonal modes which are not possible to capture by 2D simulations [29,31]. In order to reduce the computing resource requirement, 2D simulations can be used to investigate/explain the fundamental physical mechanisms that govern the detonation physics.

Although detonation simulations provide valuable insight to strengthen our comprehension of the complex detonation structure, there are still some discrepancies between the experimentally observed quantities and current state-of-the-art numerical simulations. For instance, the deviation in cell sizes, as detailed above. In fact, the discrepancy between the numerical and experimental results was not consistent and found to be case-dependent. Literature review further reveals that the documented discrepancies can be due to the modeling assumptions such as discarding the vibrational non-equilibrium effects [32], influence of the range of uncertainties over the parameters in reaction mechanism [24] and/or diffusion effects [33,34].

In this context, we have validated an OpenFOAM® solver named `reactingPimpleCentralFoam` [35–37] to perform hydrogen-based detonation simulations, within the accuracy of the current state-of-the-art numerical simulations in open literature. This solver has already been tested/verified against experiments to compute the global dynamics of detonation transmission in a curved chamber [24] (using OpenFOAM® v4.1 distribution), supersonic combustion [38] for ejector ramjet applications and detonation initiation through shock focusing [39, 40]. It is important to note that most solvers in the detonation community are closed-source in-house code and there are limited open-source options that have been properly verified and validated. The current study is devoted to careful verification and validation of the solver, to provide appropriate guidelines on the necessary grid resolution to get converged solutions and to implement efficient ways of computing the detonation structures.

In the following subsections, the numerical methodology is discussed in detail in Sec. 2 followed by the case setup in Sec. 3. Then the results are discussed in the following sequence: first, results from 1D simulations (Sec. 4.1.1 & Sec. 4.1.2) followed by 2D simulations in both weakly (Sec. 4.2.1) and moderately (Sec. 4.2.2) unstable mixtures are discussed in SFR. This is then followed by the 2D solution comparison between uniform and non-uniform grid (Sec. 4.2.3). The results from 1D simulations in LFR are summarized in the appendix (See Sec. A.1).

2. Numerical Methodology

An order of magnitude analysis reveals that the characteristic time scales associated with the convection ($\tau_{\text{conv}} \sim \Delta_i / D_{\text{CJ}}$) and chemical reaction ($\sim \tau_{\text{chem}}$) dominates around the region of detonation front over the time scales associated with the viscous ($\tau_{\text{visc}} \sim \Delta_i^2/\nu$) and heat diffusion ($\tau_{\text{heat}} \sim \Delta_i^2/\alpha$). The characteristic length scale chosen here is the induction zone length behind the shock (Δ_i). For hydrogen-air detonations at low pressures (20 – 50 kPa), Δ_i ranges from 100 – 1000 μm, $D_{\text{CJ}} \sim 2$ km/s and diffusivity is around 10^{-5} m^2/s. Roughly estimating the order of these time scales for hydrogen combustion turns out to be: $\tau_{\text{visc}}/\tau_{\text{conv}} \sim \tau_{\text{heat}}/\tau_{\text{conv}} \sim \mathcal{O}(4)$. This enables us to perform the detonation simulations by neglecting the diffusion without any significant loss in the accuracy of the solution. Therefore, all simulations conducted in this validation study utilized the Euler equations without physical diffusion effects, accomplished by setting the diffusion coefficients to zero within the solver.

2.1. Governing equations.

$$\frac{\partial}{\partial t}(\rho) + \nabla\cdot(\rho\mathbf{U}) = 0 \tag{1}$$

$$\frac{\partial}{\partial t}(\rho\mathbf{U}) + \nabla\cdot(\rho\mathbf{U}\mathbf{U}) = -\nabla p \tag{2}$$

$$\frac{\partial}{\partial t}(\rho Y_k) + \nabla\cdot(\rho\mathbf{U}Y_k) = \dot{\omega}_k \quad \text{for } k = 1...N_s \tag{3}$$

$$\frac{\partial}{\partial t}(\rho h_s) + \nabla\cdot(\rho\mathbf{U}h_s) = \dot{\omega}_T + \frac{Dp}{Dt} \tag{4}$$

$$p - \rho R_u \sum_{k=1}^{N_s} \frac{Y_k}{W_k} T = 0 \tag{5}$$

are the differential form of conservation equations for mass, momentum, species, energy and equation of state, respectively. Here, $\mathbf{U}$ indicates the velocity vector. Then, ρ, p, Y_k, $\dot{\omega}_k$ and $\dot{\omega}_T$ represents the density, pressure, mass fraction of the k^{th} species, production rate of the k^{th} species and heat release rate due to combustion, respectively. The universal gas constant is represented by R_u, the temperature by T, and the molecular weight of the k^{th} species is W_k. Note that the energy equation is solved in the sensible enthalpy form (h_s) and is related to total (h_t) and formation enthalpy (Δh_f^{o}) at reference temperature, T_{o}, as:

$$h_s \equiv \int_{T_{\text{o}}}^{T} C_p dT = h_t - \sum_{k=1}^{N_s} \Delta h_{f,k}^{\text{o}} Y_k \tag{6}$$

The specific heat capacity of the gas (C_p) at constant pressure are used from the JANAF tables [41].

2.2. Chemical kinetics and source terms.

Considering a system of M reactions comprising of N_s species can be represented as [1]:

$$\sum_{k=1}^{N_s} \nu'_{k,m} \mathcal{S}_k \underset{k_{b,m}}{\overset{k_{f,m}}{\rightleftharpoons}} \sum_{k=1}^{N_s} \nu''_{k,m} \mathcal{S}_k \quad \text{for } m = 1...M \tag{7}$$

where $\mathcal{S}_k$ is the notation for k^{th} species. $\nu'_{k,m}$ and $\nu''_{k,m}$ are the number of stoichiometric moles of the k^{th} species participating in the m^{th} reaction. Primes are used to differentiate between the reactant or product sides of the reactions. k_f and k_b indicate the reaction rate constant for the forward and backward reactions, respectively. Forward reaction rate constant for reaction m ($k_{f,m}$) is modeled by the empirical modified form of Arrhenius law in terms of the pre-exponential factor (A_m), the temperature exponent (β_m) and the activation energy (E_m) of an m^{th} reaction as:

$$k_{f,m} = A_m T^{\beta_m} \exp\left(\frac{E_m}{R_u T}\right) \tag{8}$$

The backward reaction rate constant of a given reaction is calculated from the forward rate constant and equilibrium rate constant ($K_{\text{eq,m}}$) through:

$$k_{b,m} \equiv \frac{k_{f,m}}{K_{\text{eq,m}}} \tag{9}$$

$$K_{\text{eq,m}} = \left(\frac{1 \text{ atm}}{RT}\right)^{\sum_{k=1}^{N_s} \nu''_{k,m} - \nu'_{k,m}} \exp\left[\frac{\Delta S^{\text{o}}_m}{R_u} - \frac{\Delta H^{\text{o}}_m}{R_u T}\right] \tag{10}$$

Here, the changes in entropy (ΔS^{o}_m) and enthalpy (ΔH^{o}_m) for a reaction are obtained from tabulated data as a function of temperature. At any instant, the production/consumption rate of k^{th} species is the sum of production/consumption rates, $\dot{\omega}_{k,m}$, from all M reactions. Hence, the source term in species conservation Eqn. 3 is:

$$\dot{\omega}_k = \sum_{k=1}^{N_s} \dot{\omega}_{k,m} \tag{11}$$

$$= W_k \sum_{m=1}^{M} (\nu''_{k,m} - \nu'_{k,m}) \left[k_{f,m} \prod_{k=1}^{N_s} \left(\frac{\rho_k}{W_k}\right)^{\nu'_{k,m}} - k_{b,m} \prod_{k=1}^{N_s} \left(\frac{\rho_k}{W_k}\right)^{\nu''_{k,m}}\right] \tag{12}$$

Note that here, $\rho_k = \rho Y_k$ indicates the density of the k^{th} species. The heat release term in Eqn. 4 computed from $\dot{\omega}_k$, is given by:

$$\dot{\omega}_T = -\sum_{k=1}^{N_s} \Delta h^{\text{o}}_{f,k} \dot{\omega}_k \tag{13}$$

2.3. **Numerical schemes.** The finite volume discretization schemes, available within the OpenFOAM® platform are employed in the current solver. The details of the numerical schemes used are explained in the subsequent subsections.

2.3.1. *Unsteady term.* As mentioned earlier, `reactingPimpleCentralFoam` is a pressure-based semi-implicit compressible reacting flow solver capable of performing transient simulations. In all the simulations that were performed as a part of this study, second order implicit Crank-Nicolson technique was used to discretize the unsteady term.

2.3.2. *Convective term.* In order to perform integration of divergence (or convective) terms over a discretized volume/cell in the finite volume (FV) framework, fluxes at the cell faces are required. Since the solutions are stored at the cell centroids, they need to be interpolated to get the solution at cell faces. Without excess complexity, the simplest way to perform this interpolation is to do linear interpolation between two cell centers (central differencing): an owner cell (P) and its neighbour (N), see Fig. 1. This works well for incompressible flows where the theoretical speed of sound is infinite. While for compressible flows, where the flow information propagates at the velocity of sound on top of the bulk velocity, this interpolation is not always accurate enough. The second-order semi-discrete central-upwind schemes developed by Kurganov and Tadmor (KT) [42] and Kurganov, Noelle and Petrova (KNP) [43] enable such interpolation without any requirement of exact or approximate Riemann solvers and characteristic decomposition. As stated earlier, `reactingPimpleCentralFoam` is a hybrid solver, meaning that the solver switches between the numerical schemes that are suitable for low Mach number (M) flows (i.e PISO/SIMPLE algorithm) and high Mach number flows (i.e KT/KNP algorithm). This switching is decided based on the criterion from blending function (κ_f) defined as:

$$\kappa_f = \min\left(1, \frac{M_f}{\text{Co}}\right) \tag{14}$$

Here, M_f is the Mach number at face, f and Co is the local Courant number. If the flow regime is incompressible, then $\kappa_f \to 0$ and the convective fluxes are calculated following the PISO/SIMPLE method and if $\kappa_f \to 1$, KT/KNP scheme is used. For the case at hand, the flow regime is always compressible. Hence, the solver uses KT/KNP scheme for the convective flux. In general, the integration of convective term for a cell P (refer Fig. 1) of a given volume Ω followed by application of the Gauss divergence theorem can be written as:

$$\oint_{\Omega} \nabla \cdot (\mathbf{u}\psi) dV = \oint_{\Gamma} d\mathbf{S} \cdot (\mathbf{u}\psi) \approx \sum_{f} \mathbf{S}_f \cdot \mathbf{u}_f \psi_f = \sum_{f} \phi_f \psi_f \tag{15}$$

Here, surface integration is performed over Γ and the volumetric flux associated with bulk velocity ($\mathbf{u}$) ϕ is given by $\mathbf{S}_f \cdot \mathbf{u}_f$. Based on KT/KNP scheme, the flux of any scalar transport property ψ across a given face, f, is the weighted sum of the flux contribution from both the owner and neighbor cells that share the face, f, in both positive ($+x$) and negative ($-x$) directions denoted by the subscripts f_+ and f_-, respectively. This is given by [42, 43]:

$$\sum_{f} \phi_f \psi_f = \sum_{f} \alpha_P \phi_{f_+} \psi_{f_+} + \alpha_N \phi_{f_-} \psi_{f_-} + \delta_f (\psi_{f_-} - \psi_{f_+}) \tag{16}$$

$$= \sum_{f} (\text{flux in } +x) + (\text{flux in } -x) + \text{additional flux} \tag{17}$$

This weighted sum accounts for the additional flux as indicated, if any, due to the wave propagation or discontinuity. This additional flux term is called a diffusion term [44] with a volumetric flux, δ_f. Note that the KT method, considers equal contribution of flux in both directions, hence, $\alpha_P = \alpha_N = 0.5$. While for the KNP method, weights are determined based on the speed at which the information propagates ($u \pm c$) in each direction. In this solver, the volumetric flux associated with the speed of information propagation is denoted by the symbol a_P with subscript indicating the centroid of the cell in the direction outward from P towards N:

$$a_P = \max\left(|\mathbf{S}_f| c_{f_+} + \phi_{f_+}, |\mathbf{S}_f| c_{f_-} + \phi_{f_-}, 0\right) \tag{18}$$

$$a_N = \min\left(|\mathbf{S}_f| c_{f_+} - \phi_{f_+}, -|\mathbf{S}_f| c_{f_-} + \phi_{f_-}, 0\right) \tag{19}$$

Here, $c_{f_\pm}$ is the speed of sound ($= \sqrt{(\gamma RT)_{f_\pm}}$) of the gas at the interface and γ is the adiabatic index of the gas. So the weights for KNP method are given as:

$$\alpha_P = \frac{a_P}{a_P + a_N} \tag{20}$$

$$\alpha_N = 1 - \alpha_P \tag{21}$$

$$\delta_f = \alpha_P a_N \tag{22}$$

Note that in the present study, we use the KNP method for deciding the weighing factors, α and δ. To interpolate the scalar transport, $\psi_{f_\pm}$ to the face center, second order interpolation scheme is used along with a total variation diminishing (TVD) flux limiter functions. For this specific scheme, f_+ interpolation of ψ (which could be p, T etc.) is computed as:

$$\psi_{f_+} = (1 - \mathcal{G}_{f_+})\psi_P + \mathcal{G}_{f_+} \psi_N \tag{23}$$

where $\mathcal{G} = \theta(r)(1 - \omega_f)$, $\theta(r)$ is the limiter function and r is equivalent to the ratio of successive gradients and is defined in OpenFOAM® as:

$$r = 2 \times \frac{(\nabla\psi)_P \cdot \mathbf{dx}}{\psi_N - \psi_P} - 1, \quad \text{constrained to } r \geq 0 \tag{24}$$

Note that for all the simulations that were performed in this study, we employ `van Albada` TVD limiter to limit the flux.

$$\theta(r) = \frac{r(1+r)}{1+r^2} \tag{25}$$

$$\omega_f = \left| \frac{\mathbf{S}_f \cdot (\mathbf{x}_{j+1} - \mathbf{x}_{j+1/2})}{\mathbf{S}_f \cdot (\mathbf{x}_{j+1} - \mathbf{x}_j)} \right| \tag{26}$$

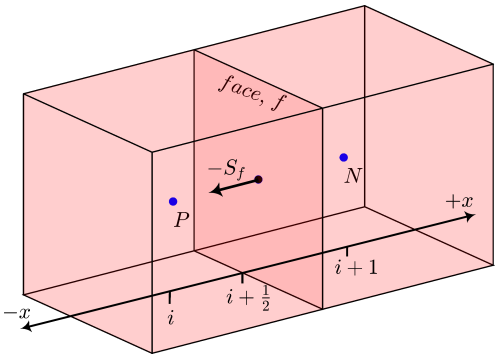

Figure 1. Schematic illustration of the flux through face, f, of area vector, $\mathbf{S}_f$, in 1D finite volume cell [36, 38, 44].

2.3.3. *Gradient term.* For the discretization of gradient terms in the governing equations, such as ∇p in Eqn. 2, we have used the standard finite volume discretization of Gaussian integration with linear interpolation of solution from cell centers to face centers.

$$\oint_{\Omega} \nabla(\psi) dV = \oint_{\Gamma} d\mathbf{S}(\psi) \approx \sum_{f} \mathbf{S}_f \psi_f \tag{27}$$

For both KT and KNP methods, the gradient terms are written as weighted sum of contribution from either directions as discussed previously for the convective terms. Then

$$\sum_{f} \mathbf{S}_f \psi_f = \sum_{f} \left(\alpha_P \mathbf{S}_f \psi_{f_+} + \alpha_N \mathbf{S}_f \psi_{f_-} \right) \tag{28}$$

As the validation cases on hydrogen detonations were inviscid reactive cases, the discretization procedures for Laplacian terms are not discussed here.

2.3.4. *ODE solver.* As the chemical time scales are usually orders of magnitude smaller in comparison to the flow time scales, it is impractical to restrict the flow solver by choosing time steps based on the smallest chemical time scale. Hence, operator splitting approach is widely used to decouple the chemical source terms ($\dot{\omega}_k$ in Eqn. 3) from the full governing equation. This is then integrated over a CFL based flow time step to compute the production rate of the species which is fed-back to the source term of the original species conservation equation. In the detailed chemistry simulations, the large range of time scales makes the system stiff and requires special solver for the integration.

In order to integrate the stiff ordinary differential equation (ODE) system, we have used `Rosenbrock34` ODE solver available in OpenFOAM®. This is an L-stable embedded Rosenbrock solver that handles stiff systems with relatively high order of accuracy (effectively of order 4) and uses adaptive time stepping internally for the time integration [45]. The summary of the numerical schemes used for the simulations to discretize each term in the governing equations is tabulated in Tab. 1.

Table 1. Summary of the numerical schemes used in the simulations

Mathematical term	Equivalent in OpenFOAM	Numerical Scheme	Order
$\partial\phi/\partial t$	`ddt`	`CrankNicolson`	$\mathcal{O}(2)_t$
$\nabla(\phi)$	`grad`	`Gauss linear`	$\mathcal{O}(2)_x$
$\nabla \cdot (\phi)$	`div`	`Gauss vanAlbada`	$\mathcal{O}(2)_x$
-	`interpolate` (reconstruction)	`linear` (`vanAlbada`)	$\mathcal{O}(2)_x$

2.3.5. *Solution and algorithm control.* For all the simulations performed in this study, we used stabilized preconditioned bi-conjugate gradient (`PBiCGStab`) method for solving the matrix equations. To ensure the invertibility of the matrices, preconditioning is performed using diagonal incomplete-Cholesky and incomplete-LU (`DILU`) method for symmetric and asymmetric matrices, respectively.

2.3.6. *Smoke foil computation.* Note that smoke foil is an experimental technique used to visualize the flow patterns and interactions of the triple shock system during the detonation propagation. As the shock wave interacts with the soot particles, it creates the cell structure on the smoke foil's surface indicating the trajectory of the triple point (defined as the point where the three shocks–Mach stem, transverse and incident shock–collide). In lab-frame simulations, this visualization is achieved through numerical computation by storing the peak pressure in a grid cell in the computational domain. For the shock-attached frame of reference (SFR) simulation, this computed field is then convected at the speed of the fresh gases from the inlet at each time step. This enables the reconstruction of the smoke foil at the end of the simulation.

3. Simulation Setup

The computational domain in 1D and 2D along with the initial and boundary conditions is discussed below.

3.1. **Computational Domain.** Figure 2a illustrates the 1D computational domain used for this study to simulate detonation in shock-attached frame of reference (SFR). The fresh gas enters the domain from the left at Chapman-Jouget (CJ) speed (indicated by the blue-colored region in Fig. 2a) followed by the initialization of the domain with the ZND solution. Note that due to `empty` boundary conditions see Fig. 2a, governing equations are not solved in the $y-$ and $z-$ directions in 1D simulations. `fixedValue` boundary condition is imposed at the inlet for all the properties and `zeroGradient` boundary condition is imposed at the outlet. Figure 2b presents the 2D computational domain for the SFR simulations. Note that the top and bottom surfaces are declared `slip walls` while all the other boundary and initial conditions are similar to that of the 1D case discussed before. We use circular hot-spots (region of $10 \times p_o$ and $10 \times T_o$) at the interface between the fresh gas and the ZND solution in the domain to disturb the initially planar (ZND) detonation structure. The size and the number of hot-spots are case-dependent and are mentioned for each mixture simulated in the subsequent sections.

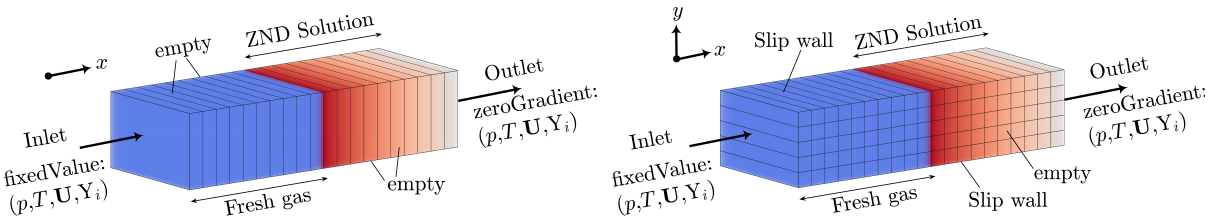

(a) 1D Computational domain **(b)** 2D Computational domain

Figure 2. Schematic illustrating the computational domain and discretization along with the boundary conditions. The colored region indicates the solution initialization at $t = 0$.

3.2. **Mixture selection.** For this validation study, we have targeted two different hydrogen-based mixture stabilities at low pressure conditions: (1) weakly unstable (WU) mixture, and (2) moderately unstable (MU) mixture. The details are given in Tab. 2. The classification of mixture stability was done based on the conventional procedure [46] implemented in shock and detonation toolbox (SDT) [47], i.e., by estimating the approximate effective activation energy [48–50] which is defined as:

$$\theta_{\text{eff}} \equiv \frac{1}{T_{\text{vN}}} \frac{\ln \tau_{-1\%} - \ln \tau_{+1\%}}{\left(\frac{1}{T_{-1\%}} - \frac{1}{T_{+1\%}}\right)} \tag{29}$$

Here, the subscripts $\pm 1\%$ denotes a perturbation about the von-Neumann temperature (T_{vN}). The induction zone length (Δ_i) indicated in Tab. 2 is obtained using the ZND solution from SDT [47]. The definition used for Δ_i is the distance between the location of the shock front and maximum heat release (or thermicity peak) from the ZND structure. In this study, all the spatial dimensions are normalized by Δ_i.

The numerical results for the mixture $2H_2 + O_2 + 10Ar$ is available in the open literature [53] while experimental results for the same condition are not available. Hence, in order to perform quantitative comparison between experiments [51] and numerical solution in terms of cell size, we have chosen the mixture $2H_2 + O_2 + 3.76Ar$. This is the rationale behind choosing two different mixtures with similar θ_{eff} in the present study.

Table 2. Summary of the stoichiometric H_2-O_2 mixtures diluted with Ar and N_2 chosen in this study. The stability parameter (θ_{eff}) is obtained from ZND simulation.

Mixture	Initial state (p_0, kPa; T_0, K)	von Neumann state (p_{vN}, kPa; T_{vN}, K)	θ_{eff}	Δ_i, μm	CJ Speed, m/s	$\bar{\lambda}$, mm
$2H_2 + O_2 + 3.76Ar$	(20, 295)	(585.8, 1937)	3.2 (WU)	240	1804	6.7 ± 0.7 [51]
$2H_2 + O_2 + 10Ar$	(45.3, 295)	(1201, 1966)	3.0 (WU)	216	1580	7 ± 3 [52]
$2H_2 + O_2 + 3.76N_2$	(20, 293)	(541.3, 1484)	4.8 (MU)	697	1935	15.2 ± 2.2 [51]

4. Results and Discussion

4.1. 1-D Results.

4.1.1. *Weakly unstable mixture.* For the mixture ($2H_2 + O_2 + 3.76Ar$), 1D simulations were performed in shock-frame of reference in a domain of length, $L_x = 417\,\Delta_i$ (corresponds to 0.1 m), with fresh gas entering the domain at CJ speed. The domain is initialized using ZND solution as shown in Fig. 3 with leading shock location at $x/\Delta_i = 0$, as indicated by the sharp discontinuity in the profiles shown in Fig. 3. The shock is followed by the von Neumann plateau in each of the profiles (see the zoomed in profiles in Fig. 3b). The simulation is advanced up to 450 μs to reach steady state, which is declared as a converged solution. This steady state solution is compared against the initial profiles. Note that for this mixture the simulations were performed on various grid systems, such that there are 16, 24, 32, 48 and 64 pts/Δ_i. Figure 4 shows the solution from the 1D SFR simulations for the weakly unstable mixture for two different grids (16 and 48 pts/Δ_i) after convergence, and the ZND solution obtained from SDT. As can be seen, the grid resolution of 16 points per induction zone length fails to capture the complete induction zone. When the domain is resolved further with 48 pts/Δ_i, the solution profile agrees well with the steady state ZND solution. Across all grid resolutions used for this mixture, the solution consistently converged to a steady state without any oscillatory behavior. This is in agreement with the stability characteristics predicted by the linear stability analysis [5] and reinforces the validity of the results. We have verified that similar results were obtained when the simulations were performed in LFR as discussed in the appendix A.1.

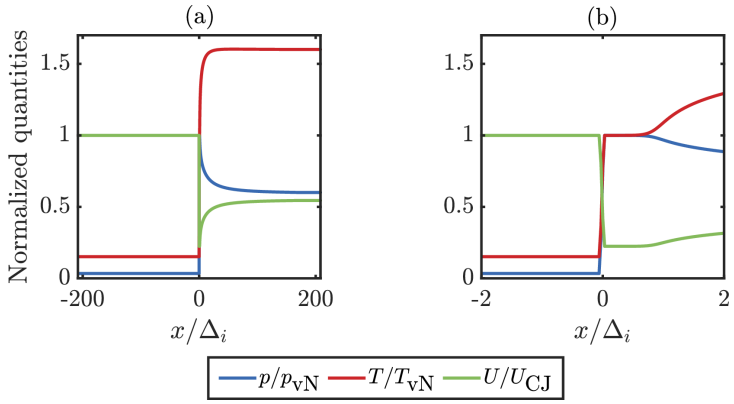

Figure 3. (a) Initial normalized profiles of pressure, temperature, and speed used for the 1D SFR simulations for the mixture $2H_2 + O_2 + 3.76Ar$ at 20 kPa and 295 K. Pressure and temperature profiles shown here are normalized by the values at von-Neumann conditions while the speed profile is normalized by the CJ speed. The zoomed view, near the detonation front, is shown in (b). Here the distance in $x-$ axis is normalized by the corresponding Δ_i.

Further, the spatial profiles of the major and minor species mass fractions from the 1D simulation with 48 pts/Δ_i are compared with the steady state ZND solution as plotted in the Fig. 5. As can be seen, the converged profiles from 1D simulation agree reasonably well with the steady state ZND solution. The temporal evolution of post-shock pressure and position of the shock front in the 1D simulation is

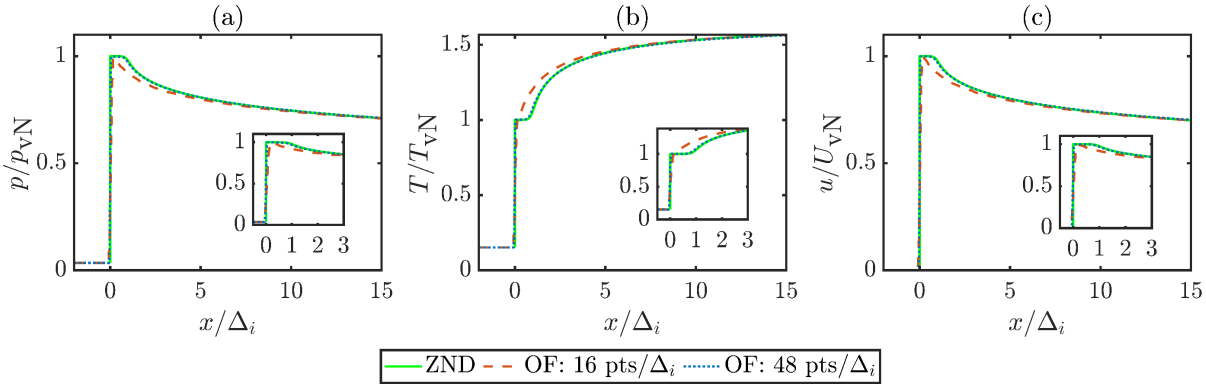

Figure 4. Comparison of normalized (a) pressure, (b) temperature and (c) speed from the 1D simulation at $t = 450\,\mu$s in shock-frame with the ZND solution for the mixture $2H_2 + O_2 + 3.76Ar$ at 20 kPa and 295 K.

plotted in the Fig. 6. As can be seen from Fig. 6a the deviation of post-shock pressure from the steady state ZND von-Neumann pressure is less than a percent over the entire duration of the computation. Also the position of the shock front does not deviate much from the initial shock position as indicated in Fig. 6b indicating that the front is propagating at the CJ speed. Furthermore, the grid convergence study revealed that there were no substantial differences observed in the obtained solution when using grid resolutions of 32, 48, and 64 pts/Δ_i. Therefore, for the selected detonation mixture, $2H_2 + O_2 + 3.76Ar$ at 20 kPa and 295 K, a grid resolution of a minimum of 32 points per induction zone length is required to achieve agreement with the steady state ZND solution.

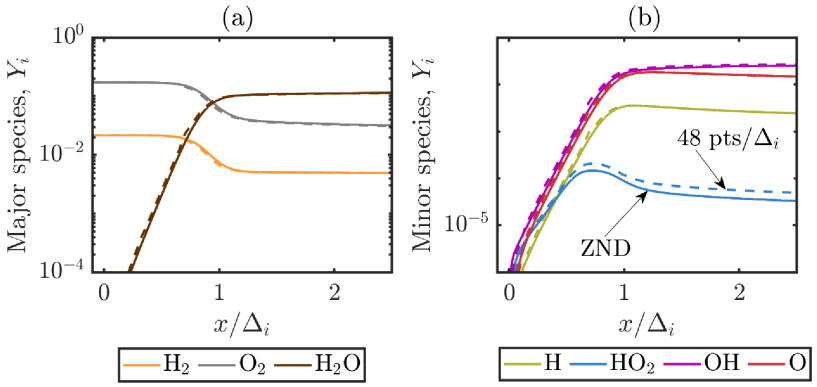

Figure 5. Comparison of mass fractions of (a) major and (b) minor species profiles of the 1D simulation (dashed line) with ZND profiles (solid line). The solution from the simulation corresponds to a grid resolution of 48 pts/Δ_i after reaching the steady state.

4.1.2. *Moderately unstable mixture.* For the mixture, $2H_2 + O_2 + 3.76N_2$, 1D simulations in SFR were performed for the same physical domain length as in the previous case ($L_x = 143\,\Delta_i$ (corresponds to 0.1 m)). The domain is initialized with solutions from a ZND simulation similar to Fig. 2a. Note that the simulations were performed on different grid systems, chosen such that there are 16, 24, 32, 48, 64, and 128 pts/Δ_i). Figure 7 displays the 1D simulation results at two different instants which is compared against the steady state ZND solution. The linear hydrodynamic stability analysis reveals that the mixture with higher effective activation energy leads to oscillating detonation in one-dimensional sense [3, 48]. The effective activation energy of the chosen mixture in case 2 lies in the unstable region based on this analysis. Hence the 1D solution is expected to show oscillating behavior at the steady state. This is observed from the 1D numerical simulations as shown in Fig. 7 from the two time instants. These two instants correspond to the extreme ends of the oscillation in a cycle. Also, note that this oscillating behavior was observed for grid resolution of $\Delta_i/48$ indicating that for this specific mixture grid size smaller than $\Delta_i/48$ is under-resolved to capture the true-stability of the mixture. During the oscillation, all the von-Neumann states and the characteristic lengths exhibit periodic variations around the ZND solution. The mass fractions of the major and some of the minor species profiles at two different

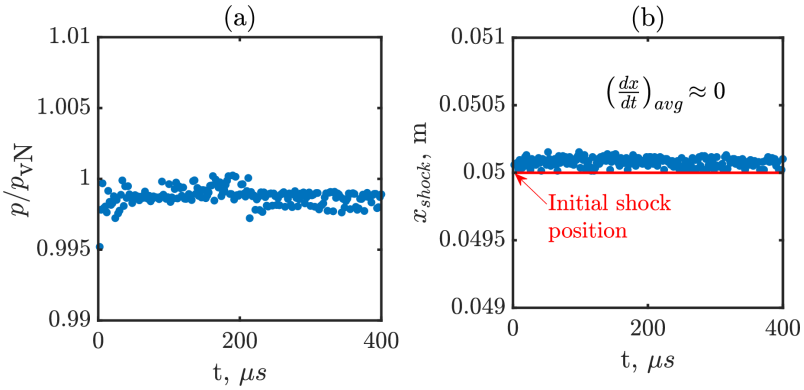

Figure 6. Temporal evolution of (a) normalized post-shock pressure, and (b) position of detonation front, from the 1D SFR simulation ($x_{\text{shock}} = 0.05\,\text{m}$ at $t = 0\,\text{s}$).

time instants are shown in the Fig. 8. Note that these profiles are adjusted based on their instantaneous shock location to compare it against the steady state ZND solution.

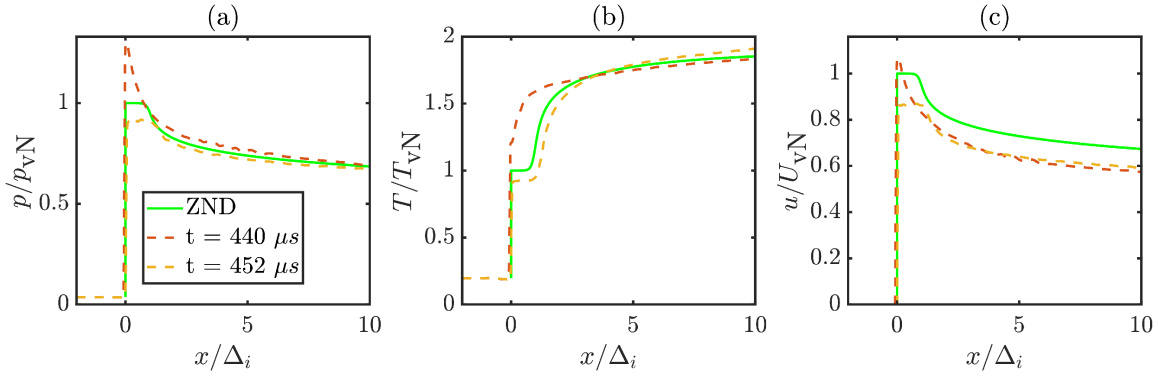

Figure 7. Comparison of normalized (a) pressure, (b) temperature and (c) velocity from the 1D simulation at two different time instants in a cycle, in shock-frame with the ZND solution for the mixture: $2H_2 + O_2 + 3.76N_2$ at 20 kPa and 295 K. The grid resolution is 48 pts/Δ_i.

When the shock position in SFR is transformed to lab frame by adding the $D_{CJ} \times t$ to the instantaneous position of the shock, the slope reveals that the average detonation propagation speed is the same as the CJ speed. Further, the variation of post-shock pressure is plotted with time in the Fig. 9b. This demonstrates the periodic nature of the solution as discussed above with post-shock pressure varying in the range from $0.9 \times p_{vN}$ to $1.3 \times p_{vN}$. The amplitude of the oscillation is a strong function of the grid system as inferred from this figure between two grids (64 and 128 pts/Δ_i).

4.2. **2-D Results.**

4.2.1. *Weakly unstable mixture.* For 2D or 3D detonation simulations, the unstable detonation structure of the front is attained typically by placing hot-spots at the start of the simulation or by distorting the initial planar structure of the detonation. These initial disturbances eventually develop into a steady propagating detonation. Note that the time taken for these initial transients to die out depends on a number of factors including, but not limited to, the number, strength, shape and position of the hot-spots, the domain size, the grid size and so on. Some of these effects were presented in [18]. All these factors influence the convergence of any detonation simulation. This poses a significant limitation on performing detonation simulations in LFR, in terms of computational power and time to converge, as the time and/or required length of the domain to reach a converged solution is not known *a priori*. Hence, an efficient alternative to reduce the computational cost is to study the detonation propagation in the SFR. Another efficient method is to use a block recycling technique like in the RESIDENT code [18,53]. Only, the former approach is considered in this work. In the present study, we ensure that each solution is independent of the initialization technique, grid size, domain size and boundary conditions (see appendix

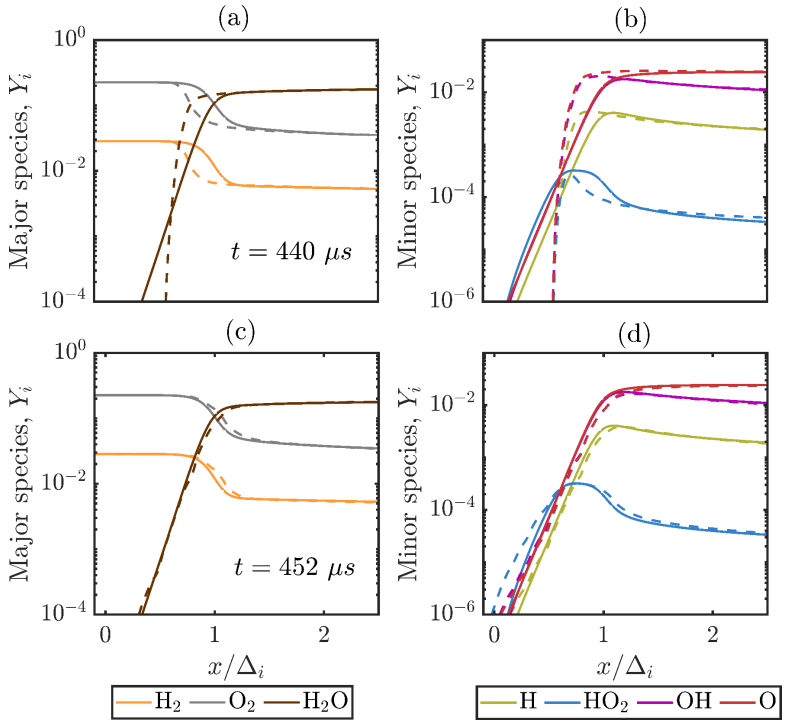

Figure 8. Comparison of mass fractions of major and minor species profiles at two time instants ((a-b) at $t = 440\,\mu s$ and (c-d) at $t = 440\,\mu s$) of the 1D simulation (dashed line) with ZND profiles (solid line). The solution from the simulation corresponds to a grid resolution of 48 pts/Δ_i after reaching the steady state.

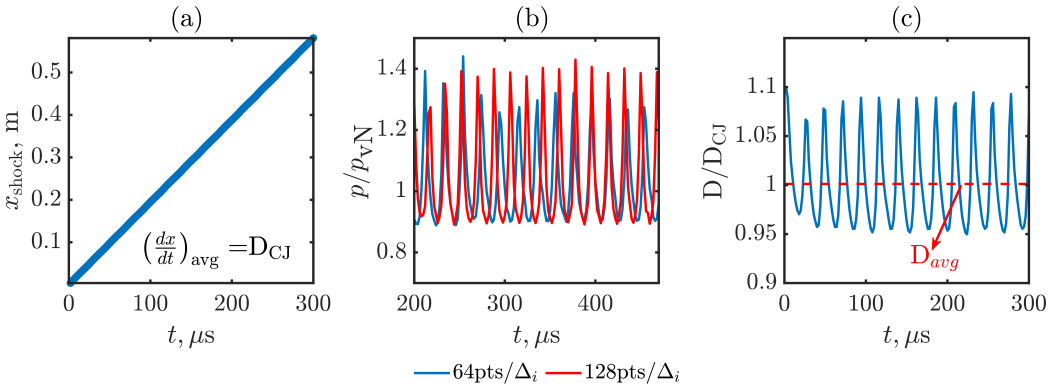

Figure 9. Temporal evolution of (a) position of the detonation front from the 1D SFR simulation (converted to lab-frame by adding $D_{CJ} \times t$), (b) normalized post-shock pressure (between two grids, 64 and 128 pts/Δ_i), and (c) gradient of x_{shock}-t curve in (a). Conditions are: $2H_2 + O_2 + 3.76N_2$ at 20 kPa and 295 K, with a grid resolution of 48 pts/Δ_i

A.2). We performed systematic studies to ensure that in all cases, although the initial transients are different, the final detonation structures are the same. For the SFR simulations with detailed chemistry, we decide the convergence by ensuring that:

- The front propagates at near CJ speed (within few percent of deviation, 2% for the present case);
- The regularity and size of cells in the smoke foil do not change drastically; achieved computing a histogram of cell widths.

The 2D simulation results for $2H_2 + O_2 + 10Ar$ mixture is discussed here. Similar to the 1D SFR simulations, the rectangular domain is initialized by stacking the 1D ZND solution throughout the width of the domain. Fresh gases enter the domain at CJ speed from the inlet on the left as shown in Fig. 10. Then a circular hot-spot (of radius $4.6\Delta_i$) of high-temperature and high-pressure zone is placed at the

middle of the domain near the front as illustrated in Fig. 10. Subsequently, the detonation evolves over time. We used $10 \times p_o$ and $10 \times T_o$ as the initial values in the circular hot-spot region in all our simulations.

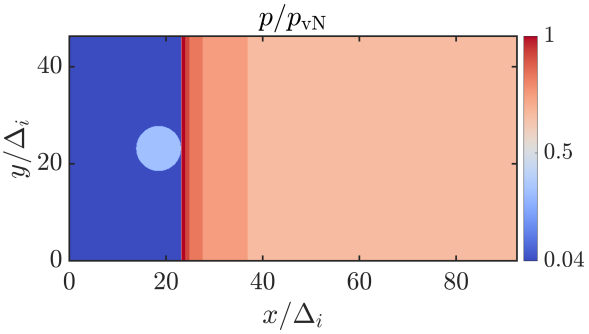

(a) Pressure (Pa) contour at $t = 0\,\mathrm{s}$ for the 2D SFR simulation on a rectangular domain

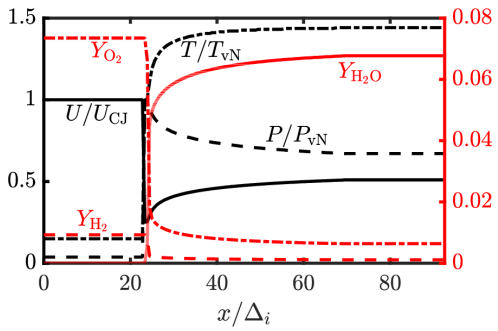

(b) ZND profiles used for initialization of the 2D domain at $t = 0\,\mathrm{s}$

Figure 10. Initial conditions for the 2D SFR simulations for the mixture $2H_2 + O_2 + 10Ar$ at 20 kPa and 295 K.

Note that for the mixture $2H_2 + O_2 + 10Ar$, the induction zone length from ZND simulation is $\approx 216\,\mu$m and the CJ speed is 1580 m/s. A quarter of the domain is initially filled with fresh gases, and as the simulation begins, a continuous inflow of fresh gases is introduced from the left inlet at the CJ speed. The CJ speed is adjusted to ensure that the detonation front remains within the domain. This adjustment is set such that the deviation from CJ speed is within ± 2%.

The simulations were conducted for a duration of up to 500 μs, except for the case with 8 pts/Δ_i, which was run for 380 μs. This time frame corresponds to approximately 3700 Δ_i of detonation propagation length (2916 Δ_i for 8 pts/Δ_i) in the laboratory frame of reference. Figure 11 shows the final 500 Δ_i of the numerical smoke foil reconstructed from the results of four different grid cases. It is worth noting that for the grid system with 8 pts/Δ_i, the detonation was over-driven ($> 1.2\ D_{CJ}$). As a result, the detonation exited the computational domain through the inlet at approximately $t = 400\,\mu$s. Hence, the solution for this specific grid was not computed further as it does not meet our convergence criteria. Also note that for the coarser grid (8 and 16 pts/Δ_i), the detonation cells are smaller in comparison to the other refined cases. This can be explained by the over-driven nature of the detonation for the coarser grid case. With further grid refinement, the cellular pattern evolves qualitatively into a similar structure for 24 and 32 pts/Δ_i for lengths above 3240 Δ_i. Thus, it can be concluded that, for the chosen mixture, a grid resolution of at least 24 pts/Δ_i is required to resolve the essential spatial structures of the 2D detonation front.

Figure 12 illustrates the 2D detonation structures from SFR simulation based on the normalized pressure p/p_{vN}, normalized temperature T/T_{vN}, the OH mass fraction Y_{OH} and the numerical schlieren fields (quantity that is a function of density gradient). All these fields enable to visualize the structure of the front with multiple triple points, each comprising a Mach stem, incident shock and transverse wave. Note that the induction zones are thinner behind the Mach stem (over-driven part of the cell) and become thicker behind the incident shock (remaining part of the cell) indicating the strong and weak coupling between the shock and reaction front, respectively. The OH mass fraction contour reveals the structure of the reaction front, characterized by keystones, which are the result of the difference in shock strengths between Mach stem and incident shock [54].

Note that although the mixture is weakly unstable, the smoke foil field shows a spectrum of length scales (cell width, λ), for which the mean cell width ($\bar{\lambda}$) is around 3.1 mm (Fig. 13). Note that the histograms do not follow a normal distribution. Hence, the mean absolute deviation (MAD(λ))–a robust measure of the spread of the data independent of the underlying distribution [55]–is used. The MAD of the cell widths in each case is asymptotically converging with grid refinement. For the initial conditions considered (45.3 kPa and 295 K with 77% of argon dilution), we were not able to find the average experimental cell width in the open literature. Hence, we decided to extrapolate the available experimental cell width from [52] to our target mixture conditions and we estimated the average cell width from experiments to be $\bar{\lambda}_{exp} = 7 \pm 3\,$mm. This uncertainty is mathematical as both the linear and exponential curve fit give out similar goodness of fit value ($R^2 = 0.99$). This means that the mean cell width from simulations deviates from the experimental value by a factor in the range of 1.3 to 3.2. This observed deviation has

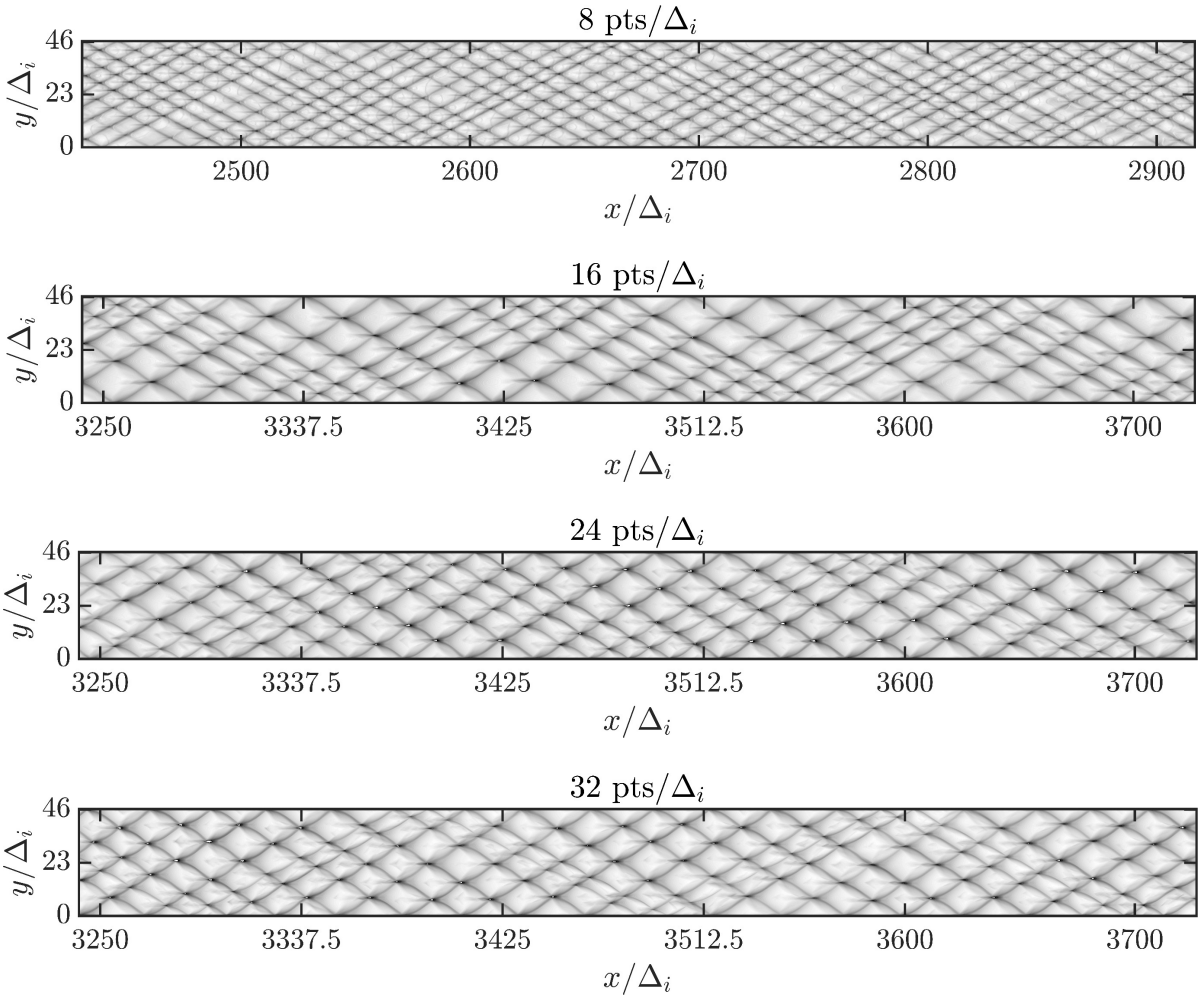

Figure 11. Reconstructed smoke foil fields from SFR detonation simulations using weakly unstable mixture: $2H_2 + O_2 + 10Ar$ at 20 kPa, for various grid systems.

been reported in several studies pertaining to detonation simulations with detailed chemistry [16,32,56]. It is also important to emphasize here that a recent study [57] reported a strong geometric (cross-sectional area of the tube) dependence of the experimental cell size at low pressure conditions.

4.2.2. *Moderately unstable mixture.* For the 2D simulations of the mixture $2H_2 + O_2 + 3.76N_2$, the same procedure as that of the previous case is followed. The domain chosen here is $85\,\Delta_i \times 65\,\Delta_i$ (60 mm × 45 mm) which is roughly 13.5 times larger in area compared to the previous domain. This is to ensure that there is a sufficient number of cells in the y–direction to make the solution independent of the wall boundaries. Circular hot-spots of radius $2.2\,\Delta_i$ are used to perturb the initially planar detonation front and a ZND solution is used as initial conditions. Note that for this specific case, the induction zone length from ZND simulation is $\approx 697\,\mu$m (based on the reduced Mével's mechanism [58]) and the CJ speed is 1935.2 m/s. A portion of the domain is initially filled with fresh gases, and as the simulation begins, a continuous inflow of fresh gases is introduced from the left inlet at the CJ speed. Unlike the previous case, the wavefront propagates at CJ speed without any deviation.

We conducted simulations on different grids due to significant changes in the cell sizes observed when using the initial three grids (16, 24 and 32 pts/Δ_i), indicating a grid-dependent solution. As we refined the grid further, we observe a consistent convergence in cell size, suggesting global asymptotic convergence. For all grids, the simulations were conducted up to 600 μs, which approximately corresponds to a meter of detonation propagation length in the laboratory frame of reference.

Figure 14 shows the final $360\,\Delta_i$ of the numerical smoke foils reconstructed from five different grids. For relatively coarse grids (16 and 24 pts/Δ_i), the cell density (defined as the effective number of cells in unit length) is high and irregular small cells are formed, compared to the more refined cases. The average cell width increases and converges to ~ 9.5 mm for the last two refined grids (40 and 48 pts/Δ_i).

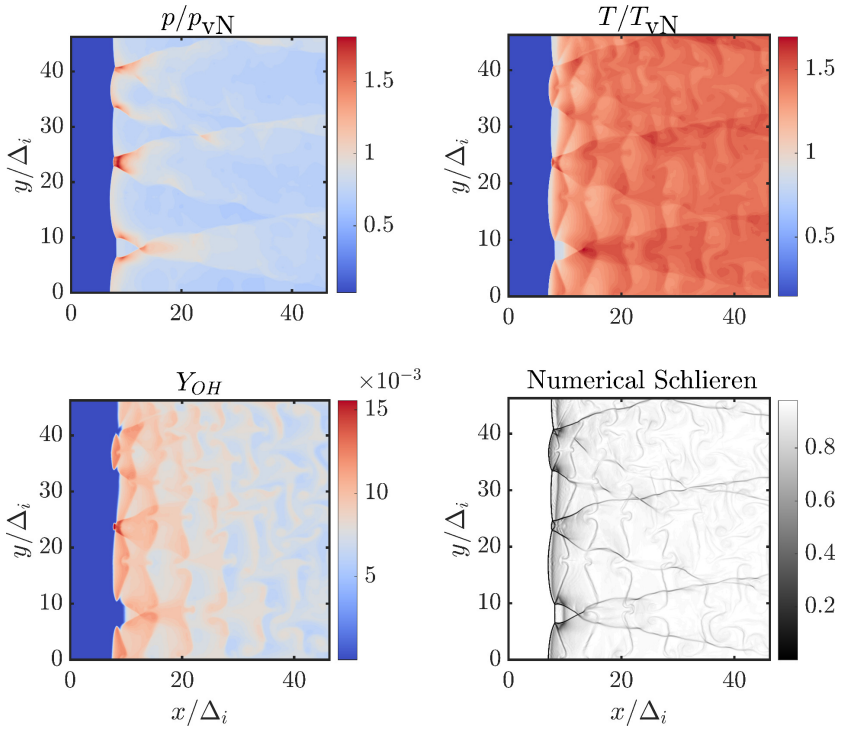

Figure 12. Contours of Pressure (top-left), temperature (top-right), mass fraction of OH (bottom-left) and numerical schlieren (bottom-right) from the detonation simulation in $2H_2 + O_2 + 10Ar$ case at 45.3 kPa and 295 K from a grid with 24 pts/Δ_i at t = 500μs. The definition used for the numerical schlieren is based on [15].

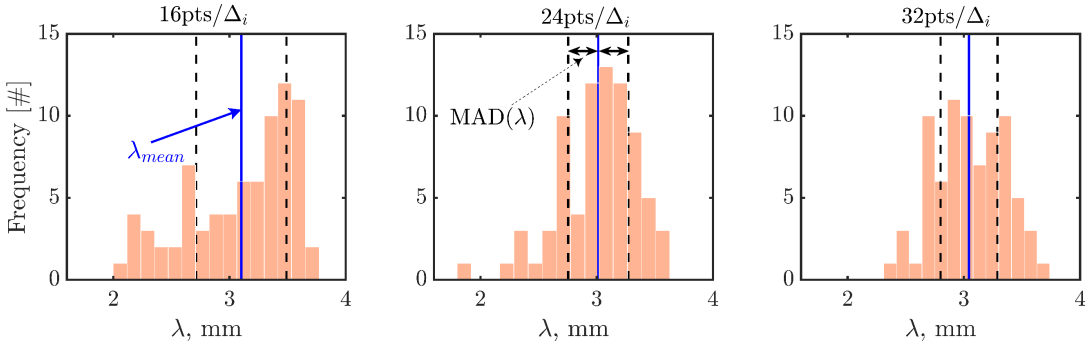

Figure 13. Histograms illustrating the distribution of cell sizes along with the mean cell width (λ_{mean}) and ±1 MAD (Mean Absolute Deviation), for various mesh cases corresponding to the weakly unstable mixture: $2H_2 + O_2 + 10Ar$. Results are extracted from the converged solutions presented in Fig. 11

The resemblance in the regularity of numerical smoke foils is clearly seen between 40 and 48 pts/Δ_i cases, indicating that the solution is independent of grid size. Thus it can be concluded that the minimum required grid size for performing simulations with this mixture is at least 40 pts/Δ_i. Fig. 15 shows the histogram of cell widths measured manually from the final two grids over 90 samples. The average cell width is $\bar{\lambda}$ = 9.75 mm and 9.35 mm for 40 and 48 pts/Δ_i, respectively. Note that the experimental $\bar{\lambda}$ measurement for the same condition is ∼15 mm [51]. So, the numerically measured mean cell width deviates from the experiments by a factor of 1.6. Similar to the weakly unstable mixture, the main features of the detonation front are obtained from the 2D fields of pressure, temperature, OH mass fraction and numerical schlieren, as shown in Fig. 16 for the nitrogen diluted mixture.

4.2.3. *Uniform and non-uniform grids.* With the aim of further reducing the computational time, we have tested one 2D simulation with a non-uniform grid from which the solutions are compared and discussed in this section. For this study, we have used $2H_2 + O_2 + 3.76Ar$ mixture at 20 kPa and 295 K.

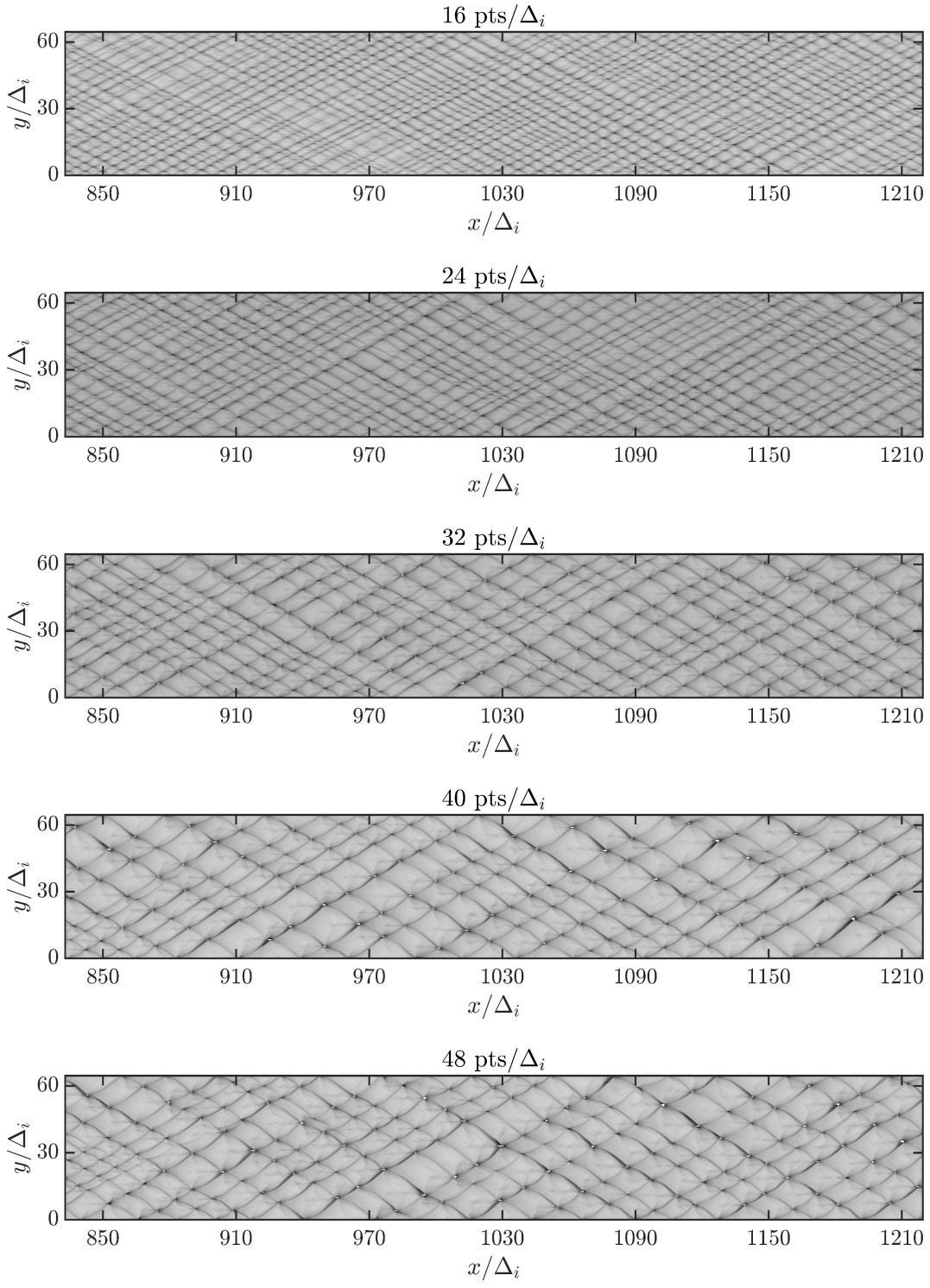

Figure 14. Reconstructed smoke foil fields from SFR detonation simulation for various grid system using weakly unstable mixture: $2H_2 + O_2 + 3.76N_2$ at 20 kPa and 295 K.

The CJ induction zone length and CJ speed from SDT for this mixture is found to be 240 μm and 1804.2 m/s, respectively. As illustrated in the previous sections, we have chosen a uniform grid system such that there are 24 pts/Δ_i in a rectangular domain of size $L_x = 64.5\,\Delta_i \times L_y = 93.8\,\Delta_i$ (15.5 mm $\times$ 22.5 mm). In the non-uniform grid system, the entire domain is divided into two regions: (i) a uniform grid for a third of the domain comprising fresh gas, shock front and $10\,\Delta_i$ behind the shock front; (ii) a non-uniform grid in the remaining portion of the domain with cell-to-cell expansion ratio of 1%. The expansion is decided based on geometric progression in the `blockMesh` utility of OpenFOAM®. Note that this alternative non-uniform grid strategy has been considered to reduce the computing time in

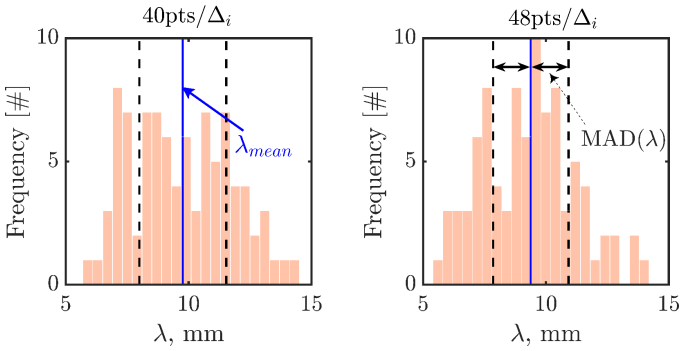

Figure 15. Histograms illustrating the distribution of cell sizes obtained with the moderately unstable mixture for 40 and 48 pts/Δ_i grid sizes. Results are extracted from the converged solutions presented in Fig. 14.

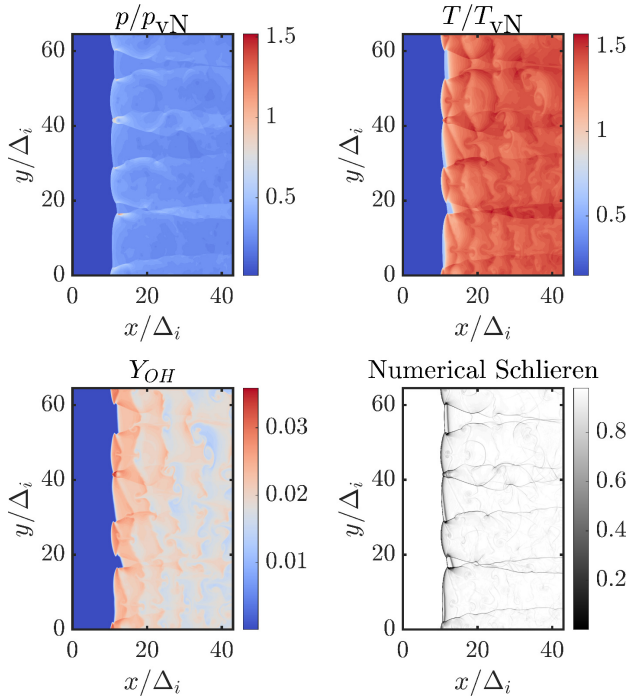

Figure 16. Contours of Pressure (top-left), temperature (top-right), mass fraction of OH (bottom-left) and numerical schlieren (bottom-right) from the detonation simulation in H_2–air case at 20 kPa and 295 K from a grid with 40 pts/Δ_i at $t = 500\,\mu$s.

comparison to the uniform grids. This section aims at highlighting the capabilities of such non-uniform meshing rather than identifying the best strategy to employ. Figure 17a shows the initial temperature field used for this set of simulations. The grid spacing along L_x is plotted in Fig. 17b. The grid spacing is normalized to display the number of cells in a Δ_i, plotted against the coordinate of the cell centroids in the $x-$direction. Two non-uniform grids are chosen such that there are 24 and 40 points per Δ_i (in the initial portion of the domain), followed by the non-uniform grid spacing.

Figure 18 compares the smoke foils obtained for uniform and non-uniform grids. This figure reveals that the cell regularity and mean cell size looks qualitatively similar among them indicating that the solution is grid independent. Note that when finer resolution is used (40 pts/Δ_i) with non-uniform grid spacing, the cell regularity and mean cell width looks qualitatively and quantitatively similar to the case with 24 pts/Δ_i resolution. Further, this can be verified from the histogram plots shown in Fig. 19. The mean cell width and mean absolute deviation for these two grids agree well with each other. We also observed that to reach a similar level of accuracy using a similar resolution, the computation time is reduced by 46% when a non-uniform grid is used compared to the uniform grid.

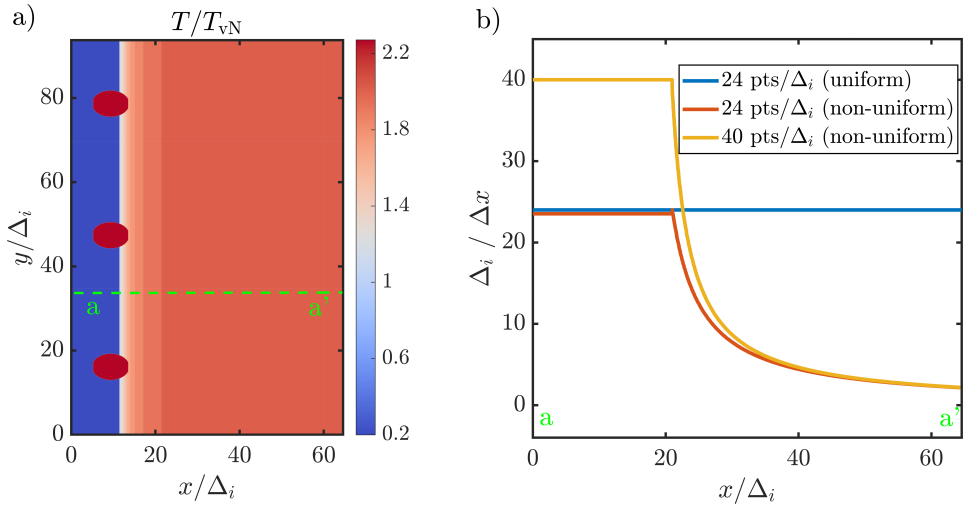

Figure 17. (a) Temperature field at $t = 0$ s for the mixture $2H_2 + O_2 + 3.76Ar$. (b) Normalized grid spacing along the line a–a' indicated in (a) for three different grids. Here Δx indicates the width of the grid cell.

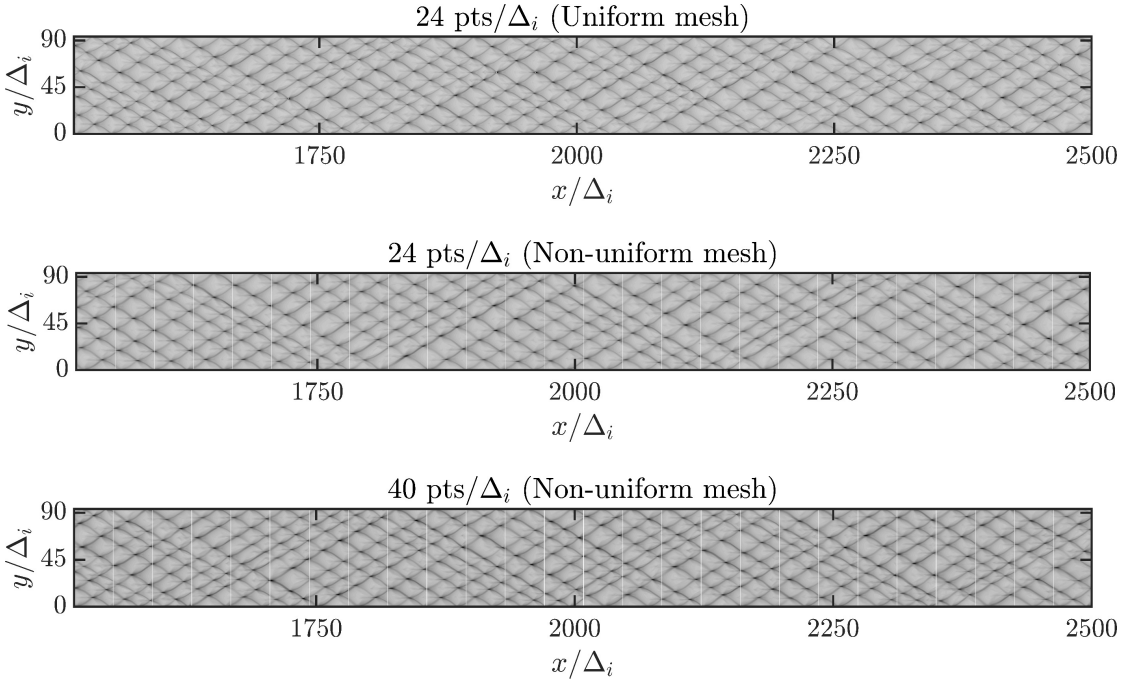

Figure 18. Reconstructed numerical smoke foils for the mixture $2H_2 + O_2 + 3.76Ar$ from three different grids: (a) uniform grid with 24 pts/Δ_i, (b) non-uniform grid with 24 pts/Δ_i near the detonation front, and (c) non-uniform grid with 40 pts/Δ_i near the detonation front.

5. Computational resource utilization

The details of the number of grid cells and corresponding number of CPU hours used for all the simulations are mentioned in the Tab. 3. In order to perform the simulations, we have used from 1 to 32 nodes, depending up on the case, with each node comprising of 32 cores.

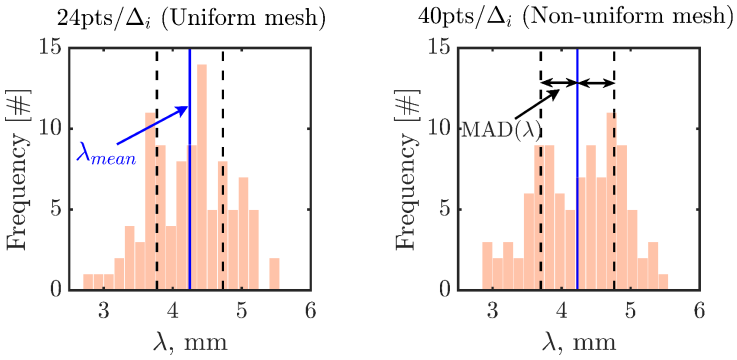

Figure 19. Histograms illustrating the distribution of cell sizes between different grid resolution corresponding to the mixture $2H_2 + O_2 + 3.76Ar$.

Table 3. Summary of CPU hours utilized for the numerical simulations performed in this study

Dimension	**Mixture**	**Grid density** (points/Δ_i)	**Number of cells** ($n_x \times n_y$)	**CPU hours**
1D	$2H_2 + O_2 + 3.76Ar$	16	$6{,}855 \times 1$	55
		32	$13{,}707 \times 1$	286
		48	$20{,}559 \times 1$	1120
		64	$27{,}411 \times 1$	2571
	$2H_2 + O_2 + 3.76N_2$	16	$2{,}319 \times 1$	55
		32	$4{,}637 \times 1$	286
		48	$6{,}955 \times 1$	169
		64	$9{,}275 \times 1$	1120
		128	$27{,}411 \times 1$	2571
2D	$2H_2 + O_2 + 10Ar$	8	743×372	26200
		16	1483×742	74300
		24	2203×1102	195,000
		32	2951×1476	296,000
	$2H_2 + O_2 + 3.76N_2$	16	1394×1046	4,300
		24	2091×1570	20,600
		32	2787×2092	140,000
		40	3484×2614	292,000
		48	4180×3136	517,000
	$2H_2 + O_2 + 3.76Ar$	24	1550×2248	75,674
		24†	745×2248	40,596
		40†	1126×3750	154,721

†Non-uniform grids (see Fig. 17(b))

6. Conclusion

This paper presents the validation of `reactingPimpleCentralFoam`, an OpenFOAM®-based hybrid-central solver, for computing hydrogen-based detonations comprising a weakly and moderately unstable mixtures. By incorporating central-upwind schemes called KT/KNP schemes to deal with the convective fluxes and leveraging the capabilities of standard OpenFOAM® solvers, the solver offers a comprehensive tool for simulating detonation phenomena.

All the one-dimensional simulations were performed in both lab-frame (LFR) and shock-attached frame of reference (SFR). With the aim of reducing the computational cost, 2D simulations were performed in shock-attached frame of reference only. We have made targeted enhancements on this solver that includes computing smoke foil field in SFR and ZND based thermicity to quantify Δ_i in 2D simulations. The latter enables numerical and experimental comparison of Δ_i for further solver and/or chemical model validation.

The validation results demonstrate the effectiveness of the solver in capturing the essential characteristics of detonation flows. In 1D simulations, the solver shows excellent agreement with the steady-state calculations of the ZND theory, for the CJ speed and the von-Neumann states, with an average error of less than 1% for all cases considered. This validation against established theoretical models confirms the reliability and accuracy of the solver for analyzing detonation processes.

The validation also extends to 2D simulations. The convergence criteria based on matching the CJ speed and achieving a steady-state cellular pattern on the numerical smoke foils further confirm the solver's ability to capture the complex dynamics of detonations.

Moreover, the computational efficiency of the SFR simulations is highlighted. Compared to LFR simulations, the SFR-based approach demonstrates superior computational efficiency while maintaining the same level of accuracy. This finding underscores the benefits of employing SFR simulations, which require fewer computational resources, in capturing the physics of detonations effectively.

We found that, for the chosen mixtures, at least 24 pts/Δ_i and 40 pts/Δ_i and a physical time of at least 500 μs are required to obtain both initialization and grid independent solutions. Note that this grid resolution also enables to resolve the fine structures of the detonation front.

Although the simulation reveals a spectrum of length scales, the mean detonation cell size ($\bar{\lambda}$) obtained from numerical smoke foils, for both the LFR and SFR simulations, are in agreement with reported detailed chemistry simulations with a deviation of a factor of at-most two from the experimental results.

Finally, further efficient usage of the resources is achieved with non-uniform grid resolution. By comparing the smoke foils results obtained from uniform and non-uniform grids, it was found that non-uniform grid reduces by 46% the computational time with the same accuracy, in terms of cell regularity and mean cell width, for the same resolution.

Acknowledgements

This research used the resources of the Supercomputing Laboratory at the King Abdullah University of Science & Technology (KAUST). This work was funded by KAUST through the baseline BAS/1/1396-01-01.

Author Contributions: Conceptualisation, V.S., K.C., J.M.-G., and D.L.; methodology, V.S., K.C., and J.M.-G.; software, J.M.-G. and V.S.; investigation, V.S.; data curation, V.S.; writing—original draft preparation, V.S.; writing—review and editing, K.C., J.M.-G., and D.L.; supervision, K.C. and J.M.-G.; funding acquisition, D.L. All authors have read and agreed to the published version of the manuscript.

Nomenclature

Acronyms

PLIF	Planar Laser-Induced Fluorescence
ZND	Zel'dovich von Neumann Döring
CJ	Chapman-Jouget
TVD	Total Variation Diminishing
KT/KNP	Kurganov-Tadmor/Kurganov-Noelle-Petrova
SFR	Shock-attached Frame of Reference
LFR	Laboratory Frame of Reference
SDT	Shock and Detonation Toolbox
vN	von-Neumann state
WU & MU	Weakly Unstable and Moderately Unstable

Symbols

λ	Detonation cell width
$\bar{\lambda}$, λ_{mean}	Mean detonation cell width
Δ_i	Induction zone length from ZND
L	Detonation cell length
τ	Induction time
τ_{conv}	Convective time scale
τ_{chem}	Chemical time scale
τ_{visc}	Viscous diffusion time scale
τ_{heat}	Thermal diffusion time scale
D_{CJ}	CJ Detonation speed
ν	Kinematic viscosity
α	Thermal diffusivity
ρ	Density of the mixture
$\mathbf{U}$	Velocity vector
p	Pressure
T	Temperature
Y_k	Mass fraction of the k^{th} species
$\dot{\omega}_k$	Reaction source of the k^{th} species
h_s	Sensible enthalpy
$\Delta h^o_{f,k}$	Formation enthalpy of the k^{th} species
h_t	Total enthalpy
$\dot{\omega}_T$	Heat release due to combustion
R_u	Universal gas constant
N_s	Number of species
W_k	Molecular weight of the k^{th} species
C_p	Specific heat capacity at constant pressure
$\nu'(\nu'')$	Stoichiometric coefficients of reactants (products)
k_f, k_b	Forward and backward reaction rate constants
E	Activation energy
A	Pre-exponential factor
β	Temperature exponent
κ_f	Blending function
M_f	Mach number at the face f
γ	Adiabatic index
Co	Acoustic Courant number
c_f	Speed of sound at the face f
$\theta(r)$	Flux limiter function
ϕ	Volumetric flux associated with bulk velocity
L_x & L_y	Length in $x-$ and $y-$ directions
n_x & n_y	Number of cells in $x-$ and $y-$ directions
θ_{eff}	Approximate effective activation energy

Appendix A.

A.1. Results from 1D lab-frame simulations.

A.1.1. *1D simulation in LFR.* The LFR 1D simulations for the mixture $2H_2 + O_2 + 3.76Ar$ at 20 kPa and 295 K in a domain of 1-m length is discussed in this section. The corresponding simulations performed in SFR is discussed in the Sec. 4.1.1. The domain is initialized with solutions from SDT's ZND simulation as shown in Fig. 20 and this 1D detonation front is allowed to propagate from right to left. Then the solution obtained at the end of the domain is compared against the initialized ZND profiles.

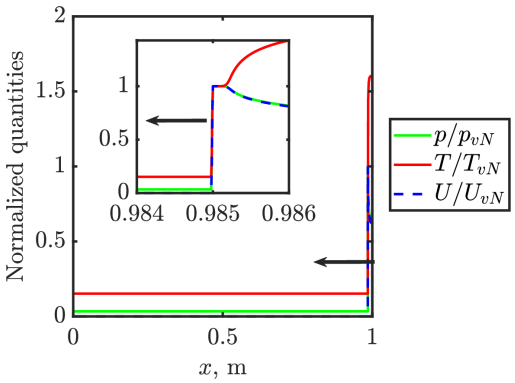

Figure 20. Initial profiles of pressure, temperature, and velocity used for the 1D LFR simulations at $t = 0$ s, for the mixture $2H_2 + O_2 + 3.76Ar$ at 20 kPa. Profiles are normalized by the values at von-Neumann conditions. Arrows indicate the direction of the detonation propagation. Zoomed view of the detonation front is shown in the figure inset.

Figure 21 compares solutions at 400 μs from 1D LFR simulations for the weakly unstable mixture ($2H_2 + O_2 + 3.76Ar$) for two different grids (16 and 48 pts/Δ_i) and the steady ZND solution obtained from SDT. The steady-state ZND solution and the OpenFOAM® solutions are in quantitative agreement. Note that the shock front is smeared for low resolution (16 pts/Δ_i), while the shock front is captured appropriately with the higher resolution (48 pts/Δ_i).

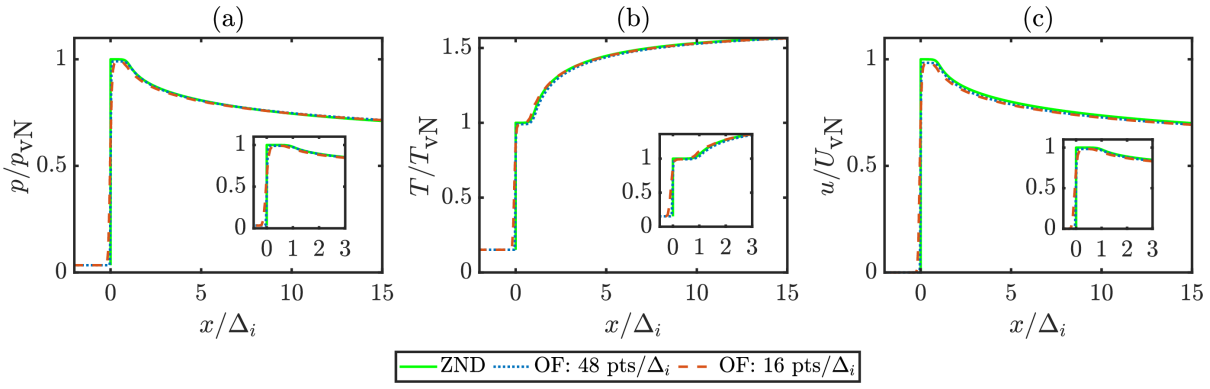

Figure 21. Comparison of normalized (a) pressure, (b) temperature, and (c) velocity profiles from the 1D simulation at $t = 400\,\mu$s in lab-frame with the ZND solution for the mixture $2H_2 + O_2 + 3.76Ar$ at 20 kPa.

The post-shock (von-Neumann state) pressure was monitored for all times, and the observed deviation of the post-shock pressure between the 1D LFR simulation and ZND is estimated to be roughly within a percent, as shown in Fig. 22a. Finally, the velocity of the detonation propagation is observed to be in reasonable agreement with the CJ velocity, with less than 2% error (see Fig. 22b). This is estimated from the slope of the $x_{\text{shock}} - t$ plot. The local slope of the $x_{\text{shock}} - t$ plot is found to vary within 2% compared to the CJ velocity from the ZND simulation as shown in the Fig. 22c. The oscillations in the plot shown in Fig. 22c can be explained by the fact that the sampling is performed every 2 μs.

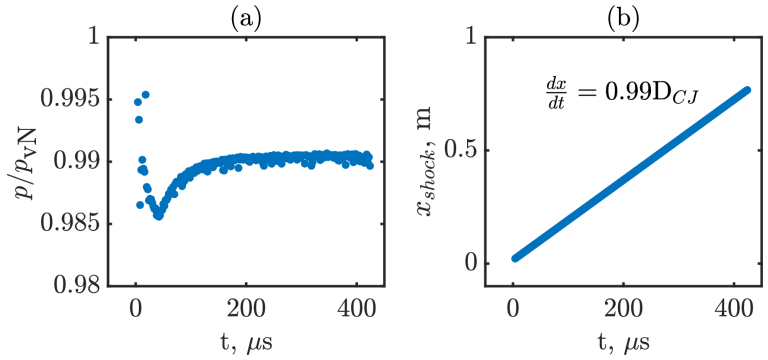

Figure 22. Time evolution of (a) normalized post-shock pressure, (b) position of the detonation front from the 1D LFR simulation.

A.1.2. *1D simulation in LFR.* For the moderately unstable mixture ($2H_2 + O_2 + 3.76N_2$), 1D simulations in lab frame of reference were performed for the same domain as in the previous case ($L_x = 1$ m). The corresponding simulation performed in SFR is discussed in Sec. 4.1.2. The domain is initialized with solutions from a ZND simulation similar to the previous case (Fig. 20). As time evolves, this 1D detonation front propagates downstream till it reaches the end of the domain. Fig. 23 displays the 1D unsteady simulation at two different instants. As explained for the SFR case in Sec. 4.1.2, the 1D simulation exhibits oscillation in the solution obtained for grids with at-least 48 pts/Δ_i. Note that this oscillating behavior was observed for grid resolution of 128 pts/Δ_i indicating that for this specific mixture grid size smaller than 128 pts/Δ_i is under-resolved to capture the true-stability of the mixture.

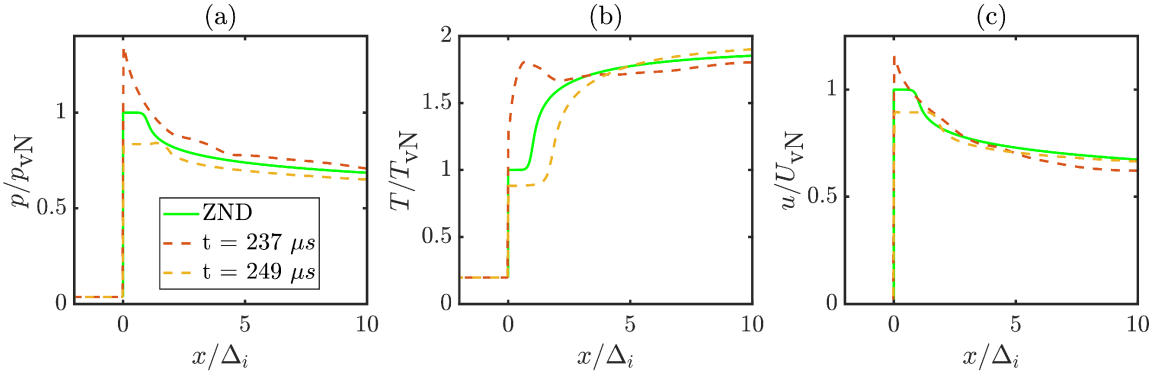

Figure 23. Comparison of normalized (a) pressure, (b) temperature, and (c) velocity from the 1D simulation at 2 different instants in a cycle, in lab-frame simulation (128 pts/Δ_i), with the ZND solution for the mixture $2H_2 + O_2 + 3.76N_2$ at 20 kPa

Figure 23 illustrates the profiles obtained from the LFR simulation at two different instants, each corresponding to maximum and minimum pressures in a cycle. As can be inferred from the temperature profiles in Fig. 23b, the induction zone length exhibits a spectrum of values indicating that the induction zone contracts and expands due to the unstable nature of the mixture arising from the stiffness in the reaction mechanism. Further analyses were performed by examining the position of the shock with time. The slope of the $x - t$ curve gives the detonation velocity and is plotted in Fig. 24. When normalized by the CJ velocity, the normalized velocity is in the range of 0.9 - 1.2. Figure 24a shows that the $x_{shock} - t$ curve is a straight line with a slope of 0.98 D_{CJ} (in linear regression sense).

A.2. **Domain dependency study.** In all the 2D simulations performed in this study, the domain size were chosen after performing systematic domain independence study. Starting with the aspect ratio of two and to accommodate at least three detonation cells, the simulations were performed to reach the converged state. If the detonation cells are converged without showing any significant changes in their sizes and regularity, the domain size is chosen for further study. We have observed in certain cases where the cell size grows along the length of the domain indicating the influence of top and bottom walls of the domain. In such cases, length in y-direction is increased gradually. Once the detonation cell size obtained between two successive domains are consistent, the former domain is chosen for further analysis.

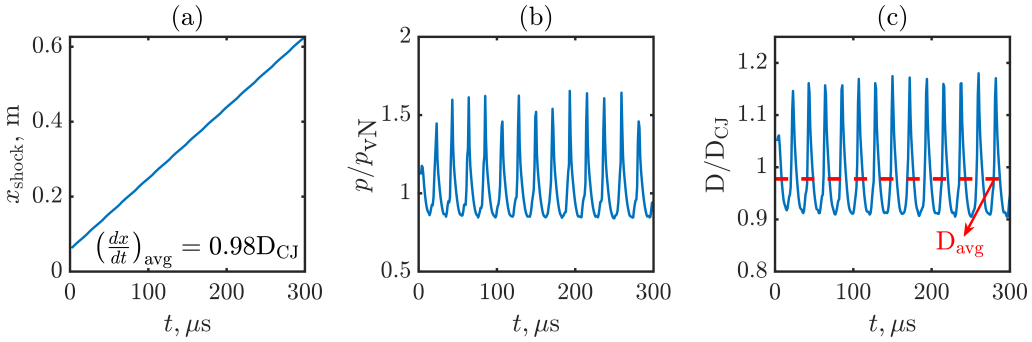

Figure 24. Temporal evolution of (a) the position of detonation front from the 1D LFR simulation, (b) the normalized post-shock pressure, and (c) the gradient of x_{shock}-t curve in *panel a*.

References

[1] T. Poinsot and D. Veynante, *Theoretical and numerical combustion.* RT Edwards, Inc., 2005. [Online]. Available: https://hal.science/hal-00270731

[2] E. S. Oran, J. P. Boris, and J. P. Boris, *Numerical simulation of reactive flow.* Citeseer, 2001, vol. 2. [Online]. Available: https://doi.org/10.1017/CBO9780511574474

[3] J. H. S. Lee, *The Detonation Phenomenon.* Cambridge University Press, 2008. [Online]. Available: https://doi.org/10.1017/CBO9780511754708

[4] E. S. Oran and J. P. Boris, "Detailed modelling of combustion systems," *Progress in Energy and Combustion Science*, vol. 7, no. 1, pp. 1–72, 1981. [Online]. Available: https://doi.org/10.1016/0360-1285(81)90014-9

[5] F. Zhang, *Shock Waves Science and Technology Library, Vol. 6: Detonation Dynamics.* Springer Science & Business Media, 2012, vol. 6. [Online]. Available: https://doi.org/10.1007/978-3-642-22967-1

[6] J. Choi, F. Ma, and V. Yang, "Some numerical issues on simulation of detonation cell structures," *Combustion, Explosion, and Shock Waves*, vol. 44, pp. 560–578, 2008. [Online]. Available: https://doi.org/10.1007/s10573-008-0086-x

[7] J. E. Shepherd, "Detonation in gases," *Proceedings of the Combustion Institute*, vol. 32, no. 1, pp. 83–98, 2009. [Online]. Available: https://doi.org/10.1016/j.proci.2008.08.006

[8] Y. Ballossier, F. Virot, and J. Melguizo-Gavilanes, "Flame acceleration and detonation onset in narrow channels: simultaneous schlieren visualization," *Combustion and Flame*, vol. 254, p. 112833, 2023. [Online]. Available: https://doi.org/10.1016/j.combustflame.2023.112833

[9] M. D. Frederick, R. M. Gejji, J. E. Shepherd, and C. D. Slabaugh, "Statistical analysis of detonation wave structure," *Proceedings of the Combustion Institute*, vol. 39, no. 3, pp. 2847–2854, 2023. [Online]. Available: https://doi.org/10.1016/j.proci.2022.08.054

[10] L. Boeck, F. Berger, J. Hasslberger, and T. Sattelmayer, "Detonation propagation in hydrogen–air mixtures with transverse concentration gradients," *Shock Waves*, vol. 26, no. 2, pp. 181–192, 2016. [Online]. Available: https://doi.org/10.1007/s00193-015-0598-8

[11] S. B. Rojas-Chavez, K. P. Chatelain, and D. A. Lacoste, "Induction zone length measurements by laser-induced fluorescence of nitric oxide in hydrogen-air detonations," *Proceedings of the Combustion Institute*, vol. 39, no. 3, pp. 2885–2894, 2023. [Online]. Available: https://doi.org/10.1016/j.proci.2022.09.020

[12] S. B. Rojas Chavez, K. P. Chatelain, and D. A. Lacoste, "Two-dimensional visualization of induction zone in hydrogen detonations," *Combustion and Flame*, vol. 255, p. 112905, 2023. [Online]. Available: https://doi.org/10.1016/j.combustflame.2023.112905

[13] S. B. Rojas-Chavez, K. P. Chatelain, T. F. Guiberti, R. Mével, and D. A. Lacoste, "Effect of the excitation line on hydroxyl radical imaging by laser induced fluorescence in hydrogen detonations," *Combustion and Flame*, vol. 229, p. 111399, 2021. [Online]. Available: https://doi.org/10.1016/j.combustflame.2021.111399

[14] E. S. Oran, J. W. Weber Jr, E. I. Stefaniw, M. H. Lefebvre, and J. D. Anderson Jr, "A numerical study of a two-dimensional H_2-O_2-Ar detonation using a detailed chemical reaction model," *Combustion and Flame*, vol. 113, no. 1-2, pp. 147–163, 1998. [Online]. Available: https://doi.org/10.1016/S0010-2180(97)00218-6

[15] C. A. Eckett, "Numerical and analytical studies of the dynamics of gaseous detonations," Ph.D. thesis, California Institute of Technology, 2001. [Online]. Available: https://resolver.caltech.edu/CaltechETD:etd-11122003-143255

[16] R. Mével, D. Davidenko, J. Austin, F. Pintgen, and J. Shepherd, "Application of a laser induced fluorescence model to the numerical simulation of detonation waves in hydrogen–oxygen–diluent mixtures," *International Journal of Hydrogen Energy*, vol. 39, no. 11, pp. 6044–6060, 2014. [Online]. Available: https://doi.org/10.1016/j.ijhydene.2014.01.182

[17] P. K. Pavalavanni, J.-E. Kim, M.-S. Jo, and J.-Y. Choi, "Numerical investigation of the detonation cell bifurcation with decomposition technique," *Aerospace*, vol. 10, no. 3, p. 318, 2023. [Online]. Available: https://doi.org/10.3390/aerospace10030318

[18] S. Taileb, J. Melguizo-Gavilanes, and A. Chinnayya, "Influence of the chemical modeling on the quenching limits of gaseous detonation waves confined by an inert layer," *Combustion and Flame*, vol. 218, pp. 247–259, 2020. [Online]. Available: https://doi.org/10.1016/j.combustflame.2020.04.018

[19] A. Sow, S.-M. Lau-Chapdelaine, and M. I. Radulescu, "Dynamics of chapman-jouguet pulsating detonations with chain-branching kinetics: Fickett's analogue and euler equations," *Proceedings of the Combustion Institute*, vol. 39, no. 3, pp. 2957–2965, 2023. [Online]. Available: https://doi.org/10.1016/j.proci.2022.11.006

[20] L. G. Marcantoni, J. Tamagno, and S. Elaskar, "Two-dimensional numerical simulations of detonation cellular structures in H_2-O_2-Ar mixtures with OpenFOAM®," *International Journal of Hydrogen Energy*, vol. 42, no. 41, pp. 26 102–26 113, 2017. [Online]. Available: https://doi.org/10.1016/j.ijhydene.2017.08.188

[21] Marcantoni, L.F. Gutiérrez and Tamagno, José and Elaskar, Sergio, "rhoCentralRfFoam: An OpenFOAM® solver for high speed chemically active flows–simulation of planar detonations–," *Computer Physics Communications*, vol. 219, pp. 209–222, 2017. [Online]. Available: https://doi.org/10.1016/j.cpc.2017.05.021

[22] Z. Huang, M. Zhao, Y. Xu, G. Li, and H. Zhang, "Eulerian-lagrangian modelling of detonative combustion in two-phase gas-droplet mixtures with openfoam: Validations and verifications," *Fuel*, vol. 286, p. 119402, 2021. [Online]. Available: https://doi.org/10.1016/j.fuel.2020.119402

[23] J. Sun, Y. Wang, B. Tian, and Z. Chen, "detonationfoam: An open-source solver for simulation of gaseous detonation based on OpenFOAM®," *Computer Physics Communications*, vol. 292, p. 108859, 2023. [Online]. Available: https://doi.org/10.1016/j.cpc.2023.108859

[24] J. Melguizo-Gavilanes, V. Rodriguez, P. Vidal, and R. Zitoun, "Dynamics of detonation transmission and propagation in a curved chamber: a numerical and experimental analysis," *Combustion and Flame*, vol. 223, pp. 460–473, 2021. [Online]. Available: https://doi.org/10.1016/j.combustflame.2020.09.032

[25] Z.-J. Xia, M.-Y. Luan, X.-Y. Liu, and J.-P. Wang, "Numerical simulation of wave mode transition in rotating detonation engine with OpenFOAM®," *International Journal of Hydrogen Energy*, vol. 45, no. 38, pp. 19 989–19 995, 2020. [Online]. Available: https://doi.org/10.1016/j.ijhydene.2020.05.100

[26] G. J. Sharpe, "Transverse waves in numerical simulations of cellular detonations," *Journal of Fluid Mechanics*, vol. 447, pp. 31–51, 2001. [Online]. Available: https://doi.org/10.1017/S0022112001005535

[27] D.-R. Cho, S.-H. Won, J.-R. Shin, and J.-Y. Choi, "Numerical study of three-dimensional detonation wave dynamics in a circular tube," *Proceedings of the Combustion Institute*, vol. 34, no. 2, pp. 1929–1937, 2013. [Online]. Available: https://doi.org/10.1016/j.proci.2012.08.003

[28] F. Toshi and R. K. Viswanath, "Propagation mechanism of detonation: three-dimensional phenomena," *Memoirs of the Faculty of Engineering, Nagoya University*, vol. 41, no. 1, pp. 93–111, 1989. [Online]. Available: https://doi.org/10.18999/memfenu.41.1.93

[29] D. N. Williams, L. Bauwens, and E. S. Oran, "Detailed structure and propagation of three-dimensional detonations," in *Symposium (International) on Combustion*, vol. 26, no. 2. Elsevier, 1996, pp. 2991–2998. [Online]. Available: https://doi.org/10.1016/S0082-0784(96)80142-1

[30] J. Crane, J. T. Lipkowicz, X. Shi, I. Wlokas, A. M. Kempf, and H. Wang, "Three-dimensional detonation structure and its response to confinement," *Proceedings of the Combustion Institute*, vol. 39, no. 3, pp. 2915–2923, 2023. [Online]. Available: https://doi.org/10.1016/j.proci.2022.10.019

[31] K. Eto, N. Tsuboi, and A. K. Hayashi, "Numerical study on three-dimensional CJ detonation waves: detailed propagating mechanism and existence of OH radical," *Proceedings of the Combustion Institute*, vol. 30, no. 2, pp. 1907–1913, 2005. [Online]. Available: https://doi.org/10.1016/j.proci.2004.08.169

[32] B. Taylor, D. Kessler, V. Gamezo, and E. Oran, "The influence of chemical kinetics on the structure of hydrogen-air detonations," in *50th AIAA Aerospace Sciences Meeting including the New Horizons Forum and Aerospace Exposition*, 2012, p. 979. [Online]. Available: https://doi.org/10.2514/6.2012-979

[33] M. I. Radulescu, "A detonation paradox: Why inviscid detonation simulations predict the incorrect trend for the role of instability in gaseous cellular detonations?" *Combustion and Flame*, vol. 195, pp. 151–162, 2018. [Online]. Available: https://doi.org/10.1016/j.combustflame.2018.05.002

[34] K. Mazaheri, Y. Mahmoudi, and M. I. Radulescu, "Diffusion and hydrodynamic instabilities in gaseous detonations," *Combustion and Flame*, vol. 159, no. 6, pp. 2138–2154, 2012. [Online]. Available: https://doi.org/10.1016/j.combustflame.2012.01.024

[35] M. Kraposhin, "unicfdlab/hybridcentralsolvers," https://github.com/unicfdlab/hybridCentralSolvers/tree/master/OpenFOAM-4.1/reactingPimpleCentralFoam, 2017.

[36] M. V. Kraposhin, A. Bovtrikova, and S. Strijhak, "Adaptation of kurganov-tadmor numerical scheme for applying in combination with the PISO method in numerical simulation of flows in a wide range of mach numbers," *Procedia Computer Science*, vol. 66, pp. 43–52, 2015. [Online]. Available: https://doi.org/10.1016/j.procs.2015.11.007

[37] M. V. Kraposhin, M. Banholzer, M. Pfitzner, and I. K. Marchevsky, "A hybrid pressure-based solver for nonideal single-phase fluid flows at all speeds," *International Journal for Numerical Methods in Fluids*, vol. 88, no. 2, pp. 79–99, 2018. [Online]. Available: https://doi.org/10.1002/fld.4512

[38] T. E. Migadel, D. Lastiwka, A. Korobenko, and C. T. Johansen, "Validation and verification of reactingpimplecentralfoam for ejector ramjet applications," in *AIAA SCITECH 2023 Forum*, 2023, p. 1228. [Online]. Available: http://arc.aiaa.org|DOI:10.2514/6.2023-1228

[39] B. Zhang, Y. Li, and H. Liu, "Analysis of the ignition induced by shock wave focusing equipped with conical and hemispherical reflectors," *Combustion and Flame*, vol. 236, p. 111763, 2022. [Online]. Available: https://doi.org/10.1016/j.combustflame.2021.111763

[40] Z. Yang and B. Zhang, "Numerical and experimental analysis of detonation induced by shock wave focusing," *Combustion and Flame*, vol. 251, p. 112691, 2023. [Online]. Available: https://doi.org/10.1016/j.combustflame.2023.112691

[41] M. W. Chase and National Information Standards Organization (US), *NIST-JANAF thermochemical tables*. American Chemical Society Washington, DC, 1998, vol. 9.

[42] A. Kurganov and E. Tadmor, "New high-resolution central schemes for nonlinear conservation laws and convection–diffusion equations," *Journal of computational physics*, vol. 160, no. 1, pp. 241–282, 2000. [Online]. Available: https://doi.org/10.1006/jcph.2000.6459

[43] A. Kurganov, S. Noelle, and G. Petrova, "Semidiscrete central-upwind schemes for hyperbolic conservation laws and hamilton–jacobi equations," *SIAM Journal on Scientific Computing*, vol. 23, no. 3, pp. 707–740, 2001. [Online]. Available: https://doi.org/10.1137/S1064827500373413

[44] C. J. Greenshields, H. G. Weller, L. Gasparini, and J. M. Reese, "Implementation of semi-discrete, non-staggered central schemes in a colocated, polyhedral, finite volume framework, for high-speed viscous flows," *International journal for numerical methods in fluids*, vol. 63, no. 1, pp. 1–21, 2010. [Online]. Available: https://doi.org/10.1002/fld.2069

[45] G. Wanner and E. Hairer, *Solving ordinary differential equations II*. Springer Berlin Heidelberg New York, 1996, vol. 375. [Online]. Available: https://doi.org/10.1007/978-3-642-05221-7

[46] J. M. Austin, "The role of instability in gaseous detonation," Ph.D. thesis, California Institute of Technology, 2003. [Online]. Available: https://resolver.caltech.edu/CaltechETD:etd-05292003-150534

[47] S. Browne, J. Ziegler, N. Bitter, B. Schmidt, J. Lawson, and J. Shepherd, "Numerical tools for shock and detonation wave modeling," in *Tech. Rep.* Explosion Dynamics Laboratory, GALCIT Pasadena, CA USA 91125, 2021. [Online]. Available: https://shepherd.caltech.edu/EDL/PublicResources/sdt/

[48] H. Lee and D. S. Stewart, "Calculation of linear detonation instability: one-dimensional instability of plane detonation," *Journal of Fluid Mechanics*, vol. 216, pp. 103–132, 1990. [Online]. Available: https://doi.org/10.1017/S0022112090000362

[49] E. Schultz and J. Shepherd, "Validation of detailed reaction mechanisms for detonation simulation," *Explosion Dynamics Laboratory Report FM99-5*, 2000. [Online]. Available: https://resolver.caltech.edu/CaltechETD:etd-11122003-143255/CaltechGALCITFM:1999.005

[50] M. Faghih, J. Melguizo-Gavilanes, and R. Mével, "A modified lotka–volterra oscillating chemical scheme for detonation simulation," *Combustion and Flame*, vol. 254, p. 112827, 2023. [Online]. Available: https://doi.org/10.1016/j.combustflame.2023.112827

[51] K. P. Chatelain, M. AliCherif, S. B. Rojas Chavez, and D. A. Lacoste, "Nitric oxide sensitization of hydrogen detonations," in *AIAA SCITECH 2023 Forum*, 2023, p. 1877. [Online]. Available: https://doi.org/10.2514/6.2023-1877

[52] M. Kaneshige and J. Shepherd, "Detonation database," GALCIT, Technical Report FM97-8, July 1997. [Online]. Available: http://www.galcit.caltech.edu/detn_db/html/

[53] K. P. Chatelain, R. Mével, J. Melguizo-Gavilanes, A. Chinnayya, S. Xu, and D. Lacoste, "Effect of incident laser sheet orientation on the OH-PLIF imaging of detonations," *Shock Waves*, vol. 30, no. 7-8, pp. 689–702, 2020. [Online]. Available: https://doi.org/10.1007/s00193-020-00963-y

[54] F. Pintgen, C. Eckett, J. Austin, and J. Shepherd, "Direct observations of reaction zone structure in propagating detonations," *Combustion and Flame*, vol. 133, no. 3, pp. 211–229, 2003. [Online]. Available: https://doi.org/10.1016/S0010-2180(02)00458-3

[55] L. Sachs, *Applied statistics: a handbook of techniques*. Springer Science & Business Media, 2012. [Online]. Available: https://doi.org/10.1007/978-1-4612-5246-7

[56] L. Shi, H. Shen, P. Zhang, D. Zhang, and C. Wen, "Assessment of vibrational non-equilibrium effect on detonation cell size," *Combustion Science and Technology*, vol. 189, no. 5, pp. 841–853, 2017. [Online]. Available: https://doi.org/10.1080/00102202.2016.1260561

[57] V. Monnier, V. Rodriguez, P. Vidal, and R. Zitoun, "An analysis of three-dimensional patterns of experimental detonation cells," *Combustion and Flame*, vol. 245, p. 112310, 2022. [Online]. Available: https://doi.org/10.1016/j.combustflame.2022.112310

[58] J. Melguizo-Gavilanes, L. Boeck, R. Mével, and J. Shepherd, "Hot surface ignition of stoichiometric hydrogen-air mixtures," *International Journal of Hydrogen Energy*, vol. 42, no. 11, pp. 7393–7403, 2017. [Online]. Available: https://doi.org/10.1016/j.ijhydene.2016.05.095